

First Simulations of a Micro-structured Rear Wall for the KATRIN experiment

Erste Simulationen einer mikrostrukturierten Rear Wall
für das KATRIN Experiment

Master's Thesis

Tom Jonah Geigle

at the
Institute of Experimental Particle Physics (ETP)

Reviewer:	Prof. Dr. Guido Drexlin
Second Reviewer:	Prof. Dr. Christian Weinheimer
Advisor:	Dr. Dominic Fabian Hinz
Second Advisor:	Dr. Martin Descher

December 16th, 2024

Erklärung zur Selbstständigkeit

Ich versichere, dass ich diese Arbeit selbstständig verfasst habe und keine anderen als die angegebenen Quellen und Hilfsmittel benutzt habe, die wörtlich oder inhaltlich übernommenen Stellen als solche kenntlich gemacht und die Satzung des KIT zur Sicherung guter wissenschaftlicher Praxis in der gültigen Fassung vom 24.05.2018 beachtet habe.

Karlsruhe, den 16.12.2024, _____

Tom Jonah Geigle

Als Prüfungsexemplar genehmigt von

Karlsruhe, den 16.12.2024, _____

Prof. Dr. Guido Drexlin

Contents

1. Introduction	1
2. Theoretical Basics	3
2.1. Historical Overview	3
2.2. Neutrinos in the Standard Model	4
2.3. Neutrino Physics	5
2.4. Sterile Neutrinos	8
2.4.1. Definition and Motivation	8
2.4.2. eV-scale Sterile Neutrino Searches	8
2.4.3. keV-scale Sterile Neutrino Searches	9
3. Karlsruhe Tritium Neutrino Experiment (KATRIN) Setup	13
3.1. Experimental Goals and Significance	13
3.1.1. Neutrino Mass Measurement	13
3.1.2. Sterile Neutrino Search	14
3.2. Experimental Setup	15
3.2.1. Rear Section	15
3.2.2. Source and Transport Section	16
3.2.3. Spectrometers	18
3.2.4. Detector System	20
3.3. Setup for keV-scale Sterile Neutrino Search	21
3.3.1. Rear Wall Modification	21
3.3.2. Field Adjustments	21
3.3.3. Detector System	22
4. RW Scenarios to reduce Backscattering	23
4.1. Theoretical Basics of Backscattering	23
4.1.1. Elastic Scattering	23
4.1.2. Inelastic Scattering	25
4.1.3. Backscattering Coefficient	27
4.2. Possible RW Modifications	27
4.2.1. Magnetic Field Adjustments	27
4.2.2. Electric Field Adjustments	28
4.2.3. Rear Wall Material	29
4.2.4. Micro-structured Rear Wall	30

5. Modeling of the RW and Beamline	33
5.1. Basics of Geant4 based Simulations	33
5.1.1. Architecture and Core Concepts	33
5.1.2. Physics Processes	34
5.1.3. Basic Setup and minimal Architecture	34
5.2. Micro-structured Rear Wall Implementation	36
5.3. Beamline Model	38
5.3.1. Overview of TRModel	38
5.3.2. Response Matrix Formalism	39
6. Simulations of a Micro-structured RW	41
6.1. Backscattering Simulations	41
6.1.1. Introduction	41
6.1.2. Comparison of Materials and Geometries	44
6.2. Surface Activity Simulations	49
6.2.1. Tritium Deposition Mechanisms	49
6.2.2. Comparison Flat and Micro-structured Rear Wall	50
6.2.3. Comparison of Materials	52
6.2.4. Limitations and Outlook	54
6.3. Impact on the measured β -decay Spectrum	56
6.3.1. Backscattering Contribution	56
6.3.2. Activity Contribution	59
7. Conclusion	65
A. TRModel Simulation Settings	73

List of Figures

2.1.	The solar neutrino spectrum. Adopted from [6]	6
2.2.	Exclusion contours for the sterile neutrino search using the data from the first two measurement campaigns of the KATRIN experiment. [21]	9
2.3.	Exclusion curves on keV sterile neutrino dark matter. The red dot shows the 3.5 keV X-ray line. Adopted from [25]	11
2.4.	Exclusion curves of current results and projected sensitivities per phase. [27]	12
3.1.	Schematic of the tritium beta decay spectrum. The endpoint of the spectrum is determined by the mass of the electron antineutrino.	14
3.2.	Schematic of the tritium beta decay spectrum with a sterile neutrino signal. The signal would be visible as a kink in the spectrum. Adapted from [3]	15
3.3.	Schematic of the KATRIN beamline. The beamline is divided into several sections. a) is the Rear Section, b) is the Windowless Gaseous Tritium Source and c) is the Transport Section. d) and e) are the Pre-Spectrometer and the Main Spectrometer and finally f) is the Detector Section. Figure by L. Köllenberger	16
3.4.	Longitudinal tritium density profile along the WGTS and schematic of the source layout. Adapted from [35]	17
3.5.	Drawings of the DPS and CPS created in CAD software with a half-cut along the horizontal plane. Adapted from [38]	18
3.6.	Principle of a MAC-E filter	20
3.7.	Schematic of the TRISTAN detector	22
4.1.	Definition of the scattering angle θ for elastic scattering.	24
4.2.	Multiple scattering processes inside of a beryllium target. Red shows an electron terminating inside of the beryllium while blue shows an electron being backscattered after multiple scatterings inside the beryllium.	25
4.3.	Energy of the electron after elastic scattering as a function of the scattering angle for different mass numbers A of the nucleus. However, this effect is on the order of $< 10^{-3} \%$ for the low keV scale. Adopted from [10]	26
4.4.	Backscattering probability as a function of the nuclear charge	30
4.5.	Photo and optical microscope image of the pTEF, that was used as background filter at the detector. Adopted from [39]	31
5.1.	General layout of the TRModel codebase. Adopted from [25]	39

6.1. Layout of the micro-structured RW in 2D and 3D	43
6.2. Angle and energy spectrum for calculation of FPD reachable electrons	44
6.3. Backscattering probability depending on the incident energy and angle for pTEF and flat geometry for Beryllium and Silicon	45
6.4. Outgoing angle distribution of all backscattered electrons independent of the energy and input angle (uniform distributions for energy in [100 eV, 18 600 eV], and $\cos \theta$ in $[-1, 0]$). $\cos \theta = 1$ ($\theta = 0^\circ$) is parallel to the field lines (z-axis) in the direction toward the KATRIN detector and $\cos \theta = 0$ ($\theta = 90^\circ$) is perpendicular to the field lines.	46
6.5. Comparison of different materials and geometries in terms of backscattering probability. A first-order distinction is shown between all backscattered electrons and those that are expected to originate from the WGTS	48
6.6. Starting height distribution for flat and pTEF RW for silicon with ratio plot of all started electrons and electrons leaving the RW	51
6.7. Energy distributions of surface activity simulations of pTEF and flat RW	52
6.8. Comparison of the starting height of electrons leaving the RW for beryllium and silicon	53
6.9. Comparison of the final energy of electrons reaching leaving the RW for beryllium and silicon	53
6.10. Comparison of the energy distribution of secondary electrons leaving the RW for beryllium and silicon	54
6.11. Comparison of the angle distribution of electrons leaving the RW for beryllium and silicon	55
6.12. Activity matrices for flat and pTEF RWs for silicon and beryllium. These are used as an input for TRModel.	55
6.13. Comparison between simulations used in current TRModel and simulations developed in the context of this thesis	57
6.14. RW contribution for only backscattering for different material and geometries	58
6.15. Sensitivity loss for different geometries and materials for only backscattering	58
6.16. Sensitivity loss for only activity	61
6.17. RW contribution for activity and backscattering	62
6.18. Sensitivity loss for backscattering and activity	62
6.19. RW contribution for activity and backscattering for activity scenarios	63
6.20. Sensitivity loss for backscattering and activity with different micro-structured scenarios	63

List of Tables

4.1. Form factors for different charge distributions. Adapted from [10]	25
A.1. TRModel components and settings for micro-structured RW simulations. . .	73
A.2. TRModel parameters used for simulations. Only backscattering and activity parameters are changed depending on the simulation. This includes the parameters amp_Bs, amp_Rw and prop_ampRw.	74

1. Introduction

The Karlsruhe Tritium Neutrino (KATRIN) experiment is at the forefront of experimental neutrino physics, aiming to measure the effective mass of the electron neutrino with unprecedented precision with a current upper limit of $m_{\nu_e} < 0.45 \text{ eV}^2$ at 90% confidence level [1]. Historically, the neutrino had been assumed to be massless, but the discovery of neutrino oscillations in the early 2000s provided the first evidence that neutrinos must possess a non-zero mass [2]. The KATRIN experiment was designed to measure the neutrino mass by studying the tritium beta decay spectrum near its endpoint. This effort, based on high-resolution spectroscopy, offers a unique window into the properties of neutrinos and their role in the Standard Model of particle physics.

Beyond the determination of neutrino mass, the KATRIN experiment is poised to expand its scientific reach through the upgrade of the detector system with the new TRISTAN detector, allowing a dedicated search for sterile neutrinos on the keV mass-scale. a hypothesized class of neutrinos that could provide a key to several outstanding questions in cosmology and particle physics. These include the nature of dark matter and mixing in the case of sterile neutrinos, the origin of the matter-antimatter asymmetry, and the mechanism behind neutrino mass generation. In the KATRIN experiment, sterile neutrinos are expected to manifest as a spectral distortion in the beta-decay spectrum of tritium. This way, it is possible to probe for the mass of sterile neutrinos in the keV range up to about 18 keV. The large activity of KATRIN's ultra-luminous tritium source allows for probing mixing angle of $\sin^2 \theta \approx 10^{-6}$ [3].

However, the TRISTAN detector upgrade is only one addition to KATRIN due to multiple other challenges that need to be overcome to achieve the required precision for the keV sterile neutrino search. Among these, the impact of electron backscattering from the rear wall, which is a critical component of the KATRIN setup, remains a significant challenge. Most electrons in KATRIN scatter off the rear wall before reaching the detector. This causes the electrons to lose energy and distort the spectrum measured at the detector. Therefore, backscattering introduces uncertainty and complicates a precise measurement.

This thesis focuses on investigating solutions to mitigate the impact of rear wall backscattering through the application of micro-structured surfaces. These surfaces, engineered

to reduce the probability of electron backscattering by enhancing absorption and scattering in controlled ways, offer a promising path toward minimizing this systematic effect. By exploring the interplay between surface properties and electron behavior, we aim to contribute to the broader effort of refining the sensitivity of KATRIN and unlocking its potential in the search for sterile neutrinos.

The following chapters will detail the theoretical foundations of sterile neutrino physics in Chapter 2, the experimental design and challenges of the KATRIN experiment, as well as the necessary changes for the sterile neutrino search in chapter 3. A detailed description of different beamline scenarios for the optimization of the KATRIN rear wall will be given in Chapter 4 and the software tools used for the simulations of the effects of these changes on the KATRIN experiment will be discussed in chapter 5. In the end, the precise setup of the simulations and their results will be presented in chapter 6, and the conclusions and outlook for future work will be given in chapter 7.

2. Theoretical Basics

Neutrinos are fundamental particles in the Standard Model, known for their tiny mass and neutral charge.

They were first proposed by Wolfgang Pauli in the 1930s to explain missing energy in beta decay [4], they were experimentally confirmed by Cowan and Reines in 1956 [5]. Neutrinos interact only through weak nuclear force and gravity, making them extremely difficult to detect. A more general overview will be given in Section 2.1.

There are three neutrino flavors - electron (ν_e), muon (ν_μ), and tau (ν_τ) - corresponding to the three generations of leptons. One of the most important discoveries in neutrino physics is flavor oscillation, where neutrinos change type as they propagate through space which implies that neutrinos have mass. This challenges the original assumptions of the Standard Model and opens new doors in particle physics. These two topics are discussed in more detail in Section 2.3.

Moreover, they provide opportunities to explore new physics, particularly through the study of sterile neutrinos, discussed further in Section 2.4.

2.1. Historical Overview

The neutrino was first postulated by Wolfgang Pauli in 1930, to explain a discrepancy in beta decay where the emitted electron seemed to lose a portion of energy in what was thought to be a two-body decay (i.e. a line spectrum was expected for the electron energy, but a continuous spectrum was observed). Pauli explained this as being due to the energy being taken away by an undetected neutral particle with nearly zero mass. [4] This turns the decay into a three-body process,

$$n \rightarrow p + e^- + \bar{\nu}_e, \tag{2.1}$$

where the decay energy is randomly distributed among the reaction products.

The direct detection of neutrinos proved to be a very difficult task because their interaction with matter is extremely weak. This finally came true when Cowan and Reines confirmed Pauli's theory in 1956 through an experiment with nuclear reactors by observing neutrinos

interacting with protons. The so-called Cowan-Reines experiment had a setup of three scintillating detector layers with two target tanks in between. The target tanks consisted of polyethylen boxes filled with a solution of water cadmium chloride. In this way they were able to detect a gamma ray stemming from the capture of the neutron produced by inverse betay decay, and two gamma rays created by pair annihilation of the positron. The reaction chain is given by [5]:



For a very long period, it was assumed that neutrinos were massless, since the generation of fermion masses requires a right-handed component. However, the Standard Model does not include right-handed neutrinos since only left-handed neutrinos have been observed due to parity violation in weak interactions. But in the late 20th century, experiments studying neutrinos from the Sun and the atmosphere were able to find fewer neutrinos than predicted, creating what was dubbed the "solar neutrino problem" [2]. In 1998, the breakthrough finally came with an experiment called the Super-Kamiokande in Japan: neutrinos were changing flavors while in flight, a process dubbed neutrino oscillation [6]. This implied that neutrinos had to have mass for oscillation to take place, so the generally held view that neutrinos were massless was wrong. It revolutionized our view on neutrinos and necessitates an update in the Standard Model. The result from Super-Kamiokande was soon after corroborated by the Sudbury Neutrino Observatory in 2001 [7]. For the discovery of neutrino mass and oscillation, Takaaki Kajita and Arthur B. McDonald received the Nobel Prize in Physics in 2015 [8, 9].

2.2. Neutrinos in the Standard Model

In the Standard Model of particle physics, neutrinos belong to a family of leptons that has two classes: neutrinos and charged leptons. Neutrinos being fermions have a spin of 1/2. Unlike their charged lepton cousins, they do not carry any electric charge. In the Standard Model, neutrinos are considered massless and interact only through the weak nuclear force and gravity. [10]

There are three generations of leptons, each generation comprising both a neutrino and a charged lepton. These are collectively known as the three neutrino flavors: the electron neutrino (ν_e), the muon neutrino (ν_μ), and the tau neutrino (ν_τ). They form left-handed weak isospin doublets with their charged lepton partners - electron, muon and tau - in the Standard Model's electroweak interaction [10]:

$$\begin{pmatrix} \nu_e \\ e^- \end{pmatrix}_L \quad \begin{pmatrix} \nu_\mu \\ \mu^- \end{pmatrix}_L \quad \begin{pmatrix} \nu_\tau \\ \tau^- \end{pmatrix}_L \tag{2.3}$$

These doublets involve the implication that neutrinos participate in the weak interactions only by their left-handed component. This stems from the observation of parity violation

in weak interactions. The neutrinos do not interact electromagnetically or strongly, since they bear no electric charge or color charge. Because of this, the detection of neutrinos is a very challenging task and usually involves huge detectors designed to capture some of the rare interactions that occur, such as the scattering of neutrinos. [10]

2.3. Neutrino Physics

Neutrino Oscillations

Neutrino oscillations are the proposed solution to the solar neutrino problem where experiments observed only about a third of the expected neutrino flux coming from the sun as previously mentioned. This spectrum is shown in figure 2.1. The idea is that neutrinos change flavor as they travel through space. This was contrary to the original assumption that neutrinos were massless and flavor eigenstates were the same as mass eigenstates. Theoretically, this is described by the Pontecorvo-Maki-Nakagawa-Sakata (PMNS) matrix and is analogous to the mixing of quark flavors in the CKM matrix [11]:

$$\begin{pmatrix} \nu_e \\ \nu_\mu \\ \nu_\tau \end{pmatrix} = U_{\text{PMNS}} \begin{pmatrix} \nu_1 \\ \nu_2 \\ \nu_3 \end{pmatrix}. \quad (2.4)$$

Here, U_{PMNS} is a unitary matrix that describes the mixing between the flavor (ν_e, ν_μ, ν_τ) and mass eigenstates (ν_1, ν_2, ν_3) [12]. The matrix can be parameterized with three mixing angles $\theta_{12}, \theta_{13}, \theta_{23}$ and a CP-violating phase δ_{CP} [11]. The matrix is named after the physicists who first proposed it: Ziro Maki, Masami Nakagawa, and Shoichi Sakata in 1962 and Bruno Pontecorvo, who suggested the idea in 1967. Multiple experiments are measuring these parameters using different neutrino sources like solar, atmospheric, reactor, and accelerator neutrinos (e.g. [13], [14], [15]). With the assumption of a plane wave, a solution for time evolution of the neutrino flavor states can be found:

$$\nu_\alpha(t) = \sum_i U_{\alpha i} e^{-iE_i t} \nu_i \quad \text{with} \quad E_i = \sqrt{p^2 + m_i^2} \quad (2.5)$$

Therefore, the probability of a neutrino of flavor α to be detected as a neutrino of flavor β after traveling a distance L is given by

$$\begin{aligned} P(\nu_\alpha \rightarrow \nu_\beta) = & \delta_{\alpha\beta} - 4 \sum_{i < j} \text{Re}(U_{\alpha i} U_{\beta i}^* U_{\alpha j}^* U_{\beta j}) \sin^2 \left(\frac{\Delta m_{ij}^2 L}{4E} \right) \\ & + 2 \sum_{i > j} \text{Im}(U_{\alpha i} U_{\beta i}^* U_{\alpha j}^* U_{\beta j}) \sin \left(\frac{\Delta m_{ij}^2 L}{2E} \right) \end{aligned} \quad (2.6)$$

under the assumption that the neutrinos are ultrarelativistic. [11] Here, $\Delta m_{ij}^2 = m_i^2 - m_j^2$ is the mass squared difference between the mass eigenstates i and j , E is the energy of the neutrino, and L is the distance traveled by the neutrino. The probability of a neutrino oscillating from one flavor to another is a function of the mixing angles $\theta_{12}, \theta_{13}, \theta_{23}$ and the CP-violating phase δ_{CP} . [11]

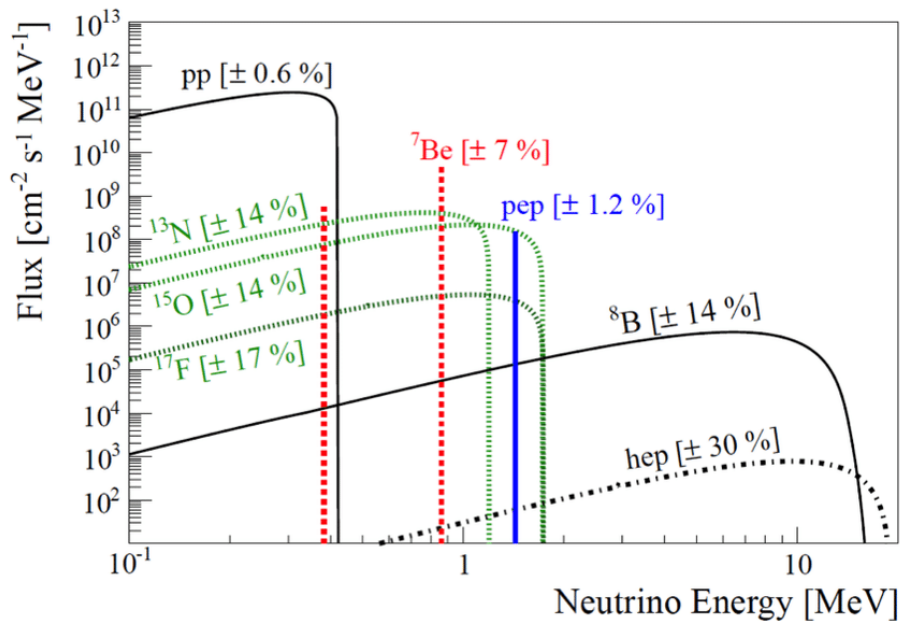


Figure 2.1.: The solar neutrino spectrum. Adopted from [6]

Dirac Neutrinos

Dirac neutrinos are one of the possible types of neutrinos. They are characterized by having distinct antiparticles, with right-handed neutrinos (ν_R) and left-handed antineutrinos ($\bar{\nu}_L$) complementing the observed left-handed neutrinos (ν_L) and right-handed antineutrinos ($\bar{\nu}_R$). These neutrinos acquire their mass through the Higgs mechanism, which requires the existence of sterile right-handed neutrinos. These sterile neutrinos do not interact via the weak force. [16]

The Dirac mass term for neutrinos is given by [16]:

$$\mathcal{L}_{\text{Dirac}} = -m_D(\bar{\nu}_L\nu_R + \bar{\nu}_R\nu_L) \quad (2.7)$$

where m_D is the Dirac mass matrix. Therefore, the neutrino mass for Dirac neutrinos is given by [16]:

$$m_D = y_D \frac{v}{\sqrt{2}} \quad (2.8)$$

where y_D is the Yukawa coupling constant and v is the vacuum expectation value of the Higgs field [16].

In addition, Dirac neutrinos follow the Dirac equation:

$$(i\gamma^\mu\partial_\mu - m)\psi = 0 \quad (2.9)$$

Here, ψ is the neutrino field.

In this way neutrino oscillations can arise from the mixing between mass eigenstates, with the conservation of the lepton number [16].

Majorana Neutrinos

Majorana neutrinos are another possible type of neutrinos. They are characterized by being their own antiparticles, which means that they are incompatible with the Standard Model (SM) of particle physics due to the violation of lepton number conservation. Mathematically, this is described by their the neutrino spinor being directly connected to their own CP-conjugate, which results in the following Lagrangian,

$$\mathcal{L}_{\text{Majorana}} = -\frac{1}{2}M_L(\bar{\nu}_L\nu_R^C + \bar{\nu}_R^C\nu_L) - \frac{1}{2}M_R(\bar{\nu}_R\nu_L^C + \bar{\nu}_L^C\nu_R) \quad (2.10)$$

where M_L and M_R are the left-handed and right-handed Majorana mass terms, respectively. The violation of the lepton number conservation also results in the impossibility to explain the creation of the Majorana mass via the SM Higgs mechanism. [16]

Seesaw Mechanism

The seesaw mechanism describes the generation of neutrino masses. The mechanism is based on the assumption that there exist additional right-handed Majorana neutrinos, which do not interact via the weak force and possess comparatively large masses [11]. The arguably simplest seesaw mechanism is the Type I seesaw mechanism, which results from the combined Dirac and Majorana mass terms under the assumption that the left-handed Majorana mass is equal to zero and the Dirac mass m_D is negligible compared to the right-handed Majorana mass M_R [11]:

$$\begin{aligned} \mathcal{L}_\nu &= -\frac{1}{2} \begin{pmatrix} \bar{\nu}_L & \bar{\nu}_L^C \end{pmatrix} \begin{pmatrix} M_L & m_D \\ m_D & M_R \end{pmatrix} \begin{pmatrix} \nu_R^C \\ \nu_R \end{pmatrix} + \text{h.c.} \\ \stackrel{M_L=0}{\Rightarrow} \mathcal{L}_\nu &= -\frac{1}{2} \begin{pmatrix} \bar{\nu}_L & \bar{\nu}_L^C \end{pmatrix} \begin{pmatrix} 0 & m_D \\ m_D & M_R \end{pmatrix} \begin{pmatrix} \nu_R^C \\ \nu_R \end{pmatrix} + \text{h.c.} \end{aligned} \quad (2.11)$$

This Lagrangian describes the mixing between left-handed neutrinos and right-handed neutrinos, with m_D being the Dirac mass matrix and M_R being the right-handed Majorana mass. Using this, it is possible to calculate the eigenvalues m_{ν_a} for the active neutrinos and m_{ν_s} for the sterile neutrinos, with the mass of the active neutrinos being much smaller than the mass of the sterile neutrinos. These two have an antiproportional relationship to each other which is the reason for the name of the seesaw mechanism. [11] In addition, these neutrinos mix with each other via the following amplitude [11]:

$$|\theta| \propto \sqrt{\frac{m_{\nu_a}}{m_{\nu_s}}} \quad (2.12)$$

2.4. Sterile Neutrinos

2.4.1. Definition and Motivation

As mentioned in section 2.3, sterile neutrinos are hypothetical particles that do not interact via the weak force, but only via gravity. The term usually refers to right-handed neutrinos, which are singlets with respect to the weak force. Their existence could explain the small mass of the active neutrinos. However, their existence has not been proven yet and is still a topic of ongoing research. [17]

In principle, sterile neutrinos can exist on any mass scale. But some mass scale, such as the eV, keV, GeV, and TeV scale can be motivated theoretically or experimentally, or both. Due to them not interacting via any of the known forces except gravity, it is only possible to detect them via mixing with regular neutrinos. Therefore, multiple different experiments are necessary to cover the full mass range of the sterile neutrinos and multiple experiments are searching for signs of their existence. [17]

The following sections will give a brief overview of some of the most important experiments and the mass range they are searching in.

2.4.2. eV-scale Sterile Neutrino Searches

There are several experiments searching for signs of sterile neutrinos in the eV-scale. Two examples will be discussed in the following.

MiniBooNE

The Mini Booster Neutrino experiment (MiniBooNE) is a neutrino oscillation experiment at Fermilab that was designed to look further into the excess of ν_e and $\bar{\nu}_e$ events observed by the LSND experiment. This excess could be explained using a $3 + N$ neutrino oscillation model which assumes three active neutrino generations with N sterile neutrinos. The experiment makes use of a neutrino beam produced in the Fermilab Booster. There 8 GeV protons collide with a Beryllium target to produce pions and kaons, which again decay into muons and neutrinos [18]. After creating the neutrinos they travel to the 541 m distant MiniBooNE detector, which is a Cherenkov detector made up of 1520 photomultiplier tubes and filled with 818 t mineral oil. Of these photomultiplier tubes, 1280 are located in the interior region and 240 are located in an optically isolated veto region. Inside the mineral oil, the neutrinos produce directed Cherenkov light and isotropic scintillation light by producing charged particles. The light is then detected by the photomultiplier tubes. [19]

The MiniBooNE collaboration has already published results in 2021 and reported a 4.8σ signal excess. However, even though the number of excess events is consistent with LSND experiment, the shape of the spectrum is not. So, most of the parameter space favored by LSND is disfavored at 95% confidence level in MiniBooNE. Therefore, analysis of the low energy is inconclusive and will need further research. [20]

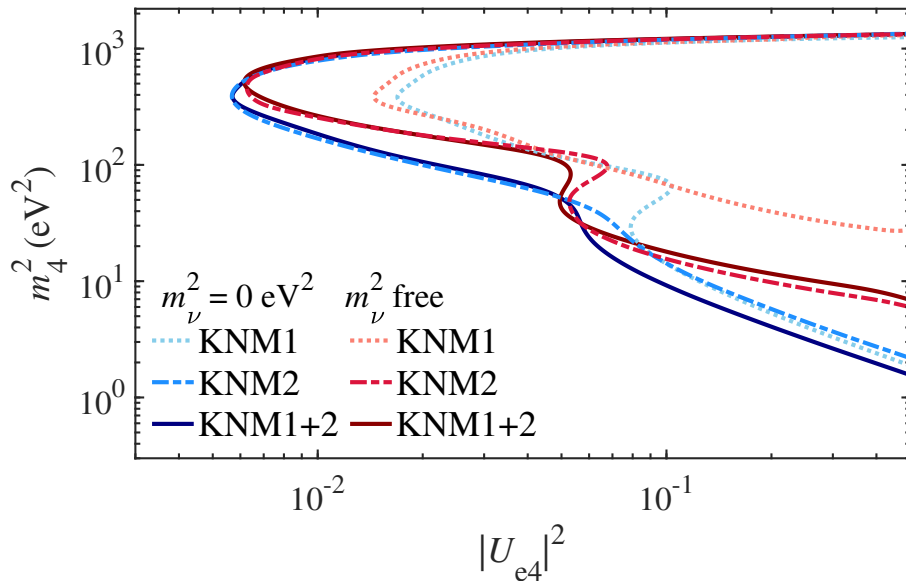


Figure 2.2.: Exclusion contours for the sterile neutrino search using the data from the first two measurement campaigns of the KATRIN experiment. [21]

KATRIN

The KATRIN experiment measures the end point of the tritium β -spectrum to determine the effective neutrino mass with high precision. Further information on the measurement principle can be found in the next chapter 3.1.1.

The shape of the beta decay spectrum is influenced by the mass states which mix with the electron neutrino. This expresses itself in a kink in the spectrum whose position is determined by the mass of the neutrino. Therefore, due to the KATRIN experiment measuring down to 40 eV below the endpoint, it is sensitive to sterile neutrinos up to $\Delta m_{41} \lesssim (40 \text{ eV})$. [21]

The KATRIN experiment has already published results in 2022 using the first two measurement campaigns. The analysis was done blind to avoid any bias and a shape analysis was used. The statistics is comprised of 3.76×10^6 signal β -electrons in the region of interest with a energy-dependent signal-to-background of up to 235. A plot of the current exclusion is shown in figure 2.2. [21]

2.4.3. keV-scale Sterile Neutrino Searches

In the case that sterile neutrinos contribute to the dark matter in the universe as dark warm matter candidates, it is possible to gain information about their mass from cosmological observations. Multiple investigations have been conducted into the existence of keV-scale sterile neutrinos using cosmological and laboratory-based observations. In the following some of the most important ones will be discussed as an example.

X-ray Observations

Sterile neutrinos on the keV mass scale are ideal candidates for dark matter (DM). If they indeed contribute to DM, their radiative decay should be observable in the cosmic

X-ray spectrum. This is due to the fact that the sterile neutrinos are able to decay into photons and active neutrinos. Even though the decay time must be several orders of magnitude greater than the age of the universe for sterile neutrinos to be a viable DM candidate, due to the sheer number of particles in view of either the Chandra or XMM-Newton observatories. Therefore, the expected signal strength would be 10^{48} s^{-1} for a cluster of galaxies halo with a mass of $10^{15} M_{\odot}$ under the assumption that the number of particles in view would be approximately 10^{78} . Because such cosmic X-rays would be unable to penetrate the Earth's atmosphere, the only way to detect them is to use space-based observatories like the previously mentioned Chandra or XMM-Newton observatories. However, the current state of X-ray observations cannot be reconciled with the thermal dark matter production limits for masses of $\gtrsim 20 \text{ keV}$, but there is still phase space left in the lower mass regions. [22] Resonant production allows for even more allowed regions, since lower values for $\sin^2 \theta$ are then possible (see figure 2.3).

In addition, during measurements, an unidentified X-ray line was observed at 3.5 keV , which could be a sign of sterile neutrinos. However, XMM-Newton as well as NuSTAR have not been able to obtain the current data to come to the conclusion that the origin of the line is not due to Dark Matter [23].

Structure Formation

Neutrinos are subject to limits from structure formation due to being candidates for warm dark matter. This is because they are relativistic at their production and then become non-relativistic so their free-streaming impedes the formation of large structures. The effect of sterile neutrinos on structure formation is dependent on their mass and momentum distribution. So, it is possible to get a lower limit on the mass of sterile neutrinos by looking at the structure formation in the universe depending on the production mechanism. This leads to a lower limit of about 10 keV for the mass of sterile neutrinos. [24]

These two examples together with several other lead to a bound on the sterile neutrino mass shown in figure 2.3.

BeEST

The Beryllium Electron Capture in Superconducting Tunnel Junctions (BeEST) experiment is another experiment with the goal of searching for sterile neutrinos. This is done by a high-precision measurement of the electron capture nuclear decay of ${}^7\text{Be}$ to ${}^7\text{Li}$. Afterwards, the final state only contains a neutrino and a recoil atom whose recoil energy is measured by a superconducting tunnel junction detector (STJ). These are a type Josephson junction that is made up of two superconducting electrodes separated by a thin insulated tunneling layer. If one of the electrodes is hit by radiation, it breaks the Cooper pairs of the ground state, which further excites the free charge carriers creating a small measurable current. The advantages of such a detector are their high maximum count rate 10^4 counts per second and their high energy resolution. In addition, their energy resolution can be easily characterized using pulsed lasers, and their response is well understood. So

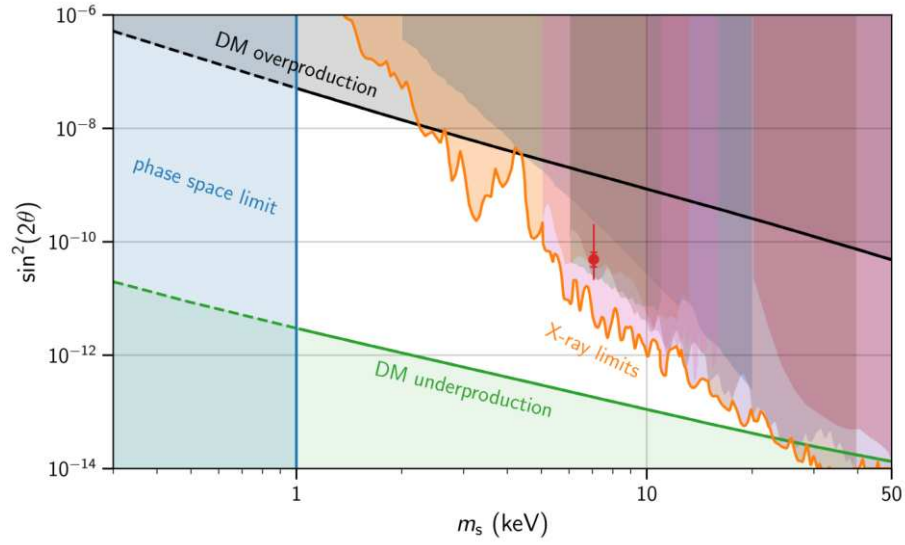


Figure 2.3.: Exclusion curves on keV sterile neutrino dark matter. The red dot shows the 3.5 keV X-ray line. Adopted from [25]

far BeEST has only published their first preliminary results from their first testing stages which is shown in Figure 2.4. [26]

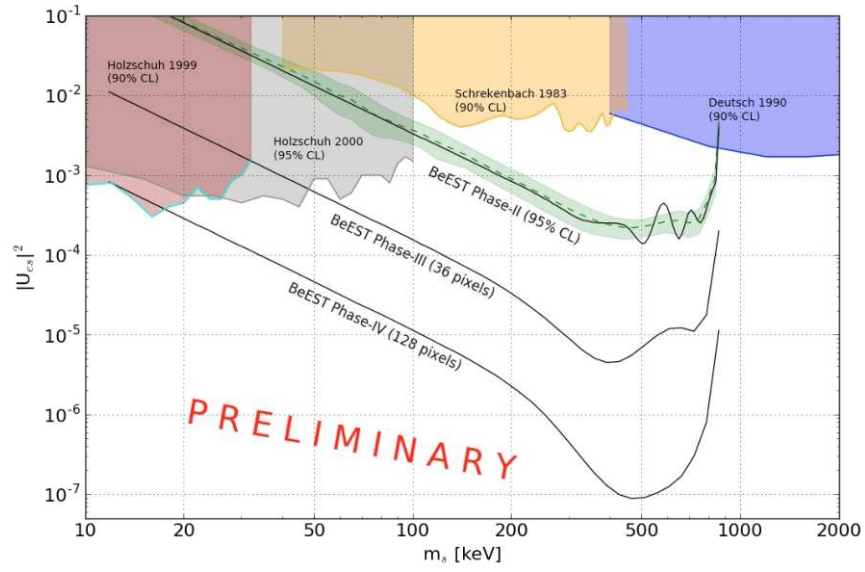


Figure 2.4.: Exclusion curves of current results and projected sensitivities per phase. [27]

3. Karlsruhe Tritium Neutrino Experiment (KATRIN) Setup

3.1. Experimental Goals and Significance

The Karlsruhe Tritium Neutrino (KATRIN) experiment has the objective to determine the effective mass of the electron antineutrino in a direct measurement. The experiment measures the energy of outgoing electrons from the decay of tritium, a beta decay process. The spectral shape near the endpoint of the tritium spectrum is influenced by the mass of the electron antineutrino. This chapter will give a brief overview of the measurement principle in Section 3.1.1 with additional information on the sterile neutrino search in section 3.1.2. The experimental setup is described in section 3.2, and section 3.3 is dedicated to future changes in the setup for the sterile neutrino search.

3.1.1. Neutrino Mass Measurement

The KATRIN experiment aims to determine the effective neutrino mass by measuring the endpoint of the tritium beta decay spectrum. In KATRIN, molecular tritium T_2 is used that decays the following way [1]:



The energy in this decay is split between the mother nucleus, the electron and the neutrino. The recoil energy of the helium can be neglected, so it is possible to assume that the energy is split randomly between electron and neutrino. The neutrinos can not be easily detected, which increases the difficulty of the neutrino mass measurement. However, their mass can be inferred by using energy momentum conservation. By measuring the energy spectrum of the electrons at the endpoint, the antineutrino mass can be determined via the missing energy. This is advantageous due to it being model-independent and only relies on the kinematics of the decay. Mathematically, the beta decay spectrum is described via the following equation [28]

$$\left(\frac{d\Gamma}{dE}\right)_{\text{nuc}} = \frac{G_F^2 |V_{ud}|^2}{2\pi^3} |M_{\text{nuc}}|^2 \cdot F(Z, E) \cdot E_e \cdot p_e \cdot E_\nu \cdot \sum_i |U_{ei}|^2 \sqrt{E_\nu^2 - m_i^2} \quad (3.2)$$

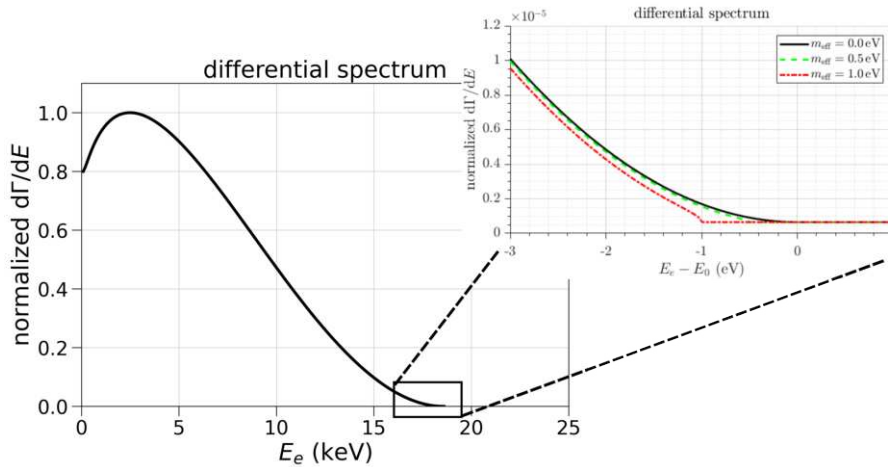


Figure 3.1.: Schematic of the tritium beta decay spectrum. The endpoint of the spectrum is determined by the mass of the electron antineutrino.

where G_f is the Fermi constant, M_{nuc} is the nuclear matrix element, and V_{ud} is the CKM matrix element. $F(Z, E)$ is the Fermi Function, which accounts for Coulomb interactions between electron and daughter nucleus. The resulting spectrum from this decay with an exaggerated neutrino mass is shown in Figure 3.1. In theory, each of the mass eigenstates of the neutrinos would show up as a kink. However, due to the limited resolution of the experiment, this cannot be resolved. Therefore, the observable squared effective antineutrino mass [28]:

$$m_{\bar{\nu}}^2 = \sum_i^3 |U_{ei}|^2 m_i^2 \quad (3.3)$$

3.1.2. Sterile Neutrino Search

After completing the neutrino mass search, the KATRIN experiment is planning to search for a signature of keV-scale sterile neutrinos as well [29]. The goal is to measure spectrum over large energy range of the differential tritium β -decay spectrum to improve current sensitivity limits for masses up to $m_s \leq E_0 = 18.6 \text{ keV}$ and up to $\sin^2 \theta < 10^{-6}$ for the sterile mixing amplitude [29]. Same as BeEST from section 2.4.3, this is also model-independent.

KATRIN's tritium source is ideal for such a search due to its high activity of about $10 \times 10^{11} \text{ Bq}$ [30]. In this way, up to 10^{18} signal electrons could be measured within three years [3]. However, this is not a rate that the current FPD detector system is able to handle, so a new detector system is needed. Therefore, the TRISTAN detector has been developed. This detector is a multi-pixel silicon drift detector array which would be able to handle up to 10^{16} electrons in a year of data taking [3]. In addition, it allows for a better energy resolution of $< 300 \text{ eV}$ FWHM in the energy region of interest.

The integration in the beamline is scheduled for 2026. The change in hardware will be discussed further in Section 3.3.

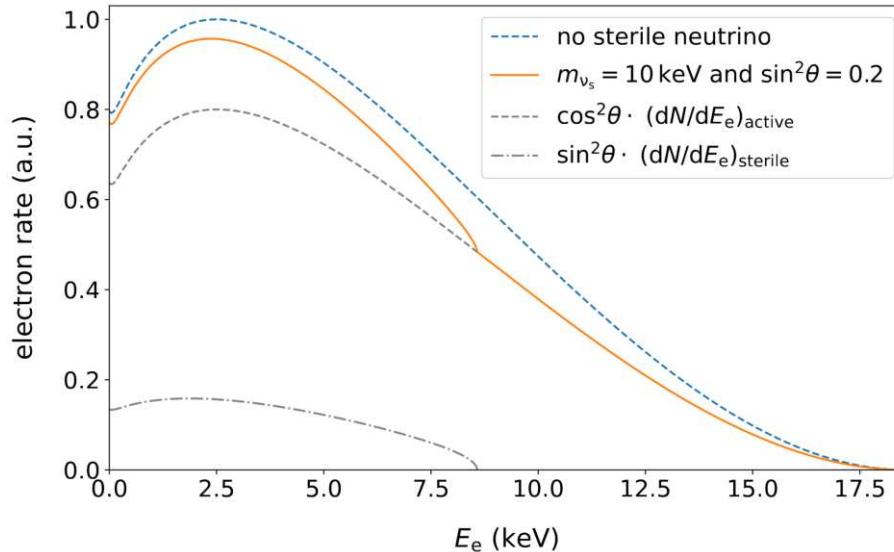


Figure 3.2.: Schematic of the tritium beta decay spectrum with a sterile neutrino signal. The signal would be visible as a kink in the spectrum. Adapted from [3]

The sterile neutrino signal would be visible as a kink in the tritium beta decay spectrum whose position and shape would be dependent on the mass m_4 and the amplitude of the mixing angle $\sin^2\theta$ of the sterile neutrino. The differential decay rate can be written as the following equation [29]:

$$\frac{d\Gamma}{dE} = \cos^2\theta \frac{d\Gamma}{dE}(m_{\bar{\nu}_e}) + \sin^2\theta \frac{d\Gamma}{dE}(m_{\nu_s}) \quad (3.4)$$

Here, $m_{\bar{\nu}_e}$ is the effective mass of the electron antineutrino and m_{ν_s} is the mass of the keV-scale sterile neutrino. In addition, $\sin^2\theta$ is the mixing amplitude of the electron neutrino flavor with the mass eigenstate introduced by the sterile neutrino. This is visualized in figure 3.2 which also indicates that KATRIN would be able to measure the sterile neutrino mass up to a mass of 18.6 keV due to the kink appearing at $E_0 - m_s$ with E_0 being the endpoint of the beta spectrum. [29]

3.2. Experimental Setup

The KATRIN experiment consists of a 70 m long beamline that is divided into several sections as seen in Figure 3.3. The sections are the source and transport section, the pre-spectrometer, the main spectrometer and the detector system. The source and transport section is responsible for the production of tritium and the transport of the tritium molecules to the main spectrometer. The pre-spectrometer is used to filter out electrons that are not in the desired energy range. The main spectrometer is used to measure the energy of the electrons and the detector system is used to detect the electrons. The setup for the sterile neutrino search is described in section 3.3. [30]

3.2.1. Rear Section

At the rear section of the KATRIN experiment is the rear wall (RW). Currently, it consists of a gold-plated steel disk with a diameter of 145 mm. The goal of the RW is to couple

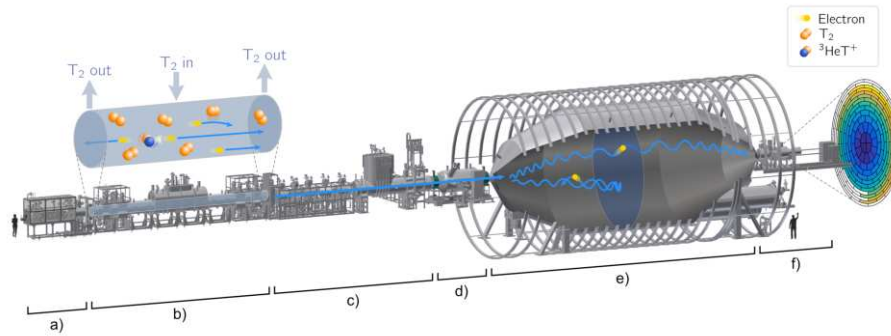


Figure 3.3.: Schematic of the KATRIN beamline. The beamline is divided into several sections. a) is the Rear Section, b) is the Windowless Gaseous Tritium Source and c) is the Transport Section. d) and e) are the Pre-Spectrometer and the Main Spectrometer and finally f) is the Detector Section. Figure by L. Köllenberger

electrically to the source plasma in order to regulate the starting potential for the β -electrons. This is necessary because of the creation of charged particles in the WGTS which would interfere with the energy measurement if left unchecked. In addition, all β -electrons created in the isotropic source that do not make it to the detector move toward the RW and are backscattered or absorbed there. This includes the electrons that are initially emitted toward the RW, but there are also some that are reflected at the maximal magnetic field further downstream, and at the retarding potential of the main spectrometer. [25, 31]

The absorption of charge carriers and neutral molecules at the RW creates one of the most significant systematic effects. This is due to the tritium adsorption at the RW which causes an additional β -decay spectrum which is also measured by the detector system. For the endpoint measurement, this can be modeled by adding a spectrum with an increased endpoint energy of $E_0 + 2 \text{ eV}$ to the WGTS spectrum [32]. One option for decontaminating the RW is ozone cleaning. For this, ozone is created by venting the system and illuminating the RW with UV-light. The ozone oxidizes the tritium molecules and other contaminants on the RW, allowing them to be pumped away. [33, 34]

The rear section also houses an electron-gun (e-gun) that shoots an electron beam through a 5 mm hole in the RW. The electrons are created photoelectrically with UV-light, accelerated using an electric field and transmitted to the FPD where they are detected. This allows the characterization of the electromagnetic fields and a measurement of the column density in the source by determining the energy loss through scattering in the WGTS. [25]

3.2.2. Source and Transport Section

The next part in the KATRIN beamline is the Windowless Gaseous Tritium Source (WGTS) which is used to produce β -electrons from tritium decay. It is a 10 m long steel tube with a diameter of 90 mm. Molecular tritium gas is injected through capillaries around the center of the tube. The gas is pumped away at the ends of the WGTS which creates an approximately linearly decreasing pressure profile along the length of the tube shown

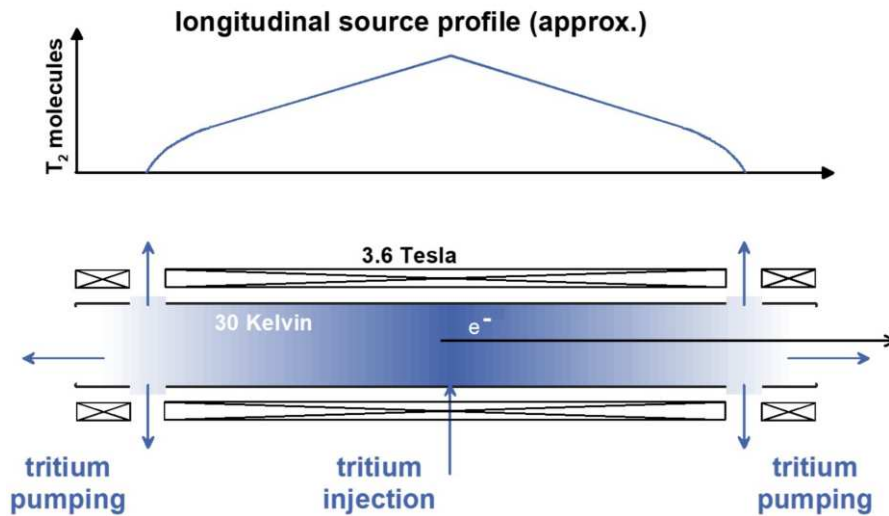


Figure 3.4.: Longitudinal tritium density profile along the WGTS and schematic of the source layout. Adapted from [35]

in Figure 3.4. It provides a flux of 10^{11} electrons per second, which are adiabatically guided along the beamline by strong magnetic fields. Its name stems from the fact that the tritium contained in the source by pumping and not by closing it off with a physical window, since this would cause significant energy loss for electrons when passing through the window material, which would distort the energy spectrum. [31, 35]

After the WGTS, the density has to be further reduced by a factor of 10^{14} to avoid contamination of the Main Spectrometer (MS) with tritium so no unwanted background is created [30]. This is achieved using a combination of the DPS and CPS.

Differential Pumping Section

The DPS consists of five superconducting magnetic solenoids which are used to guide the electrons through the section. The magnets are placed around beam tube segments that are tilted by 20° with respect to each other. In this way, a chicane is created through which the electrons are guided by the magnetic field without hindrances, while neutral or heavier particles scatter at the walls and are pumped out using multiple turbomolecular pumps. This results in a reduction of the tritium density by a factor of 10^5 . The layout of the DPS is shown in figure 3.5a. [30, 36]

In addition, the DPS is equipped with three dipole electrodes. These are used to reduce positively charged helium ions and tritium - originating from the β -decay or scattering by deflecting them towards the beamtube walls with an $\vec{E} \times \vec{B}$ drift. [36]

Cryogenic Pumping Section

Even though the the DPS is able to reduce the pressure and tritium density significantly, further reduction is necessary to avoid contamination of the MS. This is achieved using cryo-sorption. For this, the beamtube inside the CPS is cooled to 3 K and its surface is greatly increased by covering it with a structure of fine fins. To further increase the sticking

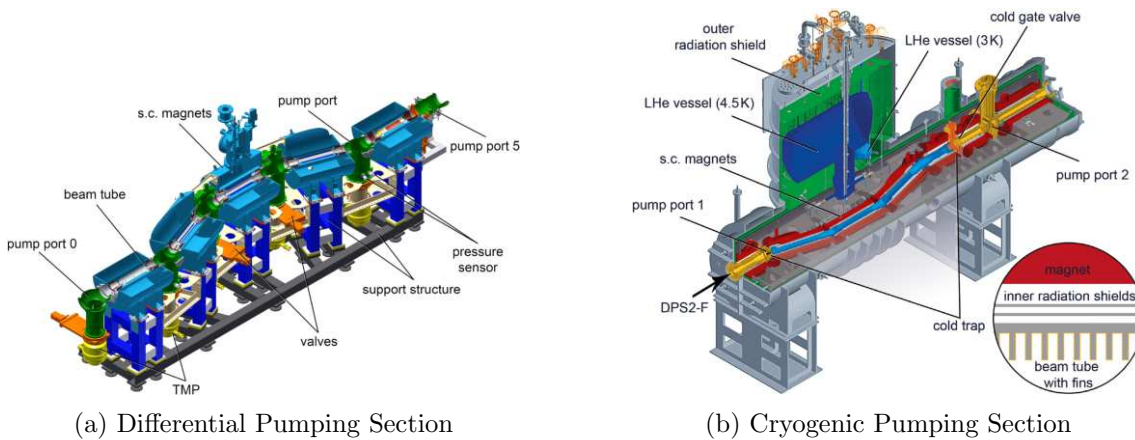


Figure 3.5.: Drawings of the DPS and CPS created in CAD software with a half-cut along the horizontal plane. Adapted from [38]

probability for tritium, the surface is covered with a thin layer of argon frost. Hence, it is necessary to maintain a very low temperature of 3 K at the surface of the CPS to increase the adsorption time. In addition, the CPS segments are, similar to the DPS segments, tilted by 15° . This is done to avoid a direct line of sight so that the tritium molecules scatter at the walls and are adsorbed, while β -electrons are able to pass through due to the guiding magnetic fields. This results in a drop off of the tritium density of seven orders of magnitude. However, due to accumulation of tritium on the argon frost layer, there is a saturation effect after a certain time, which means that the CPS has to be cleared by heating it up in regular intervals. Afterwards, the argon layer is renewed. The layout of the CPS is shown in figure 3.5b. [30, 37]

3.2.3. Spectrometers

The Pre-Spectrometer and Main Spectrometer used in the KATRIN experiment work by using Magnetic Adiabatic Collimation with Electrostatic filtering (MAC-E). They essentially act as a high-pass filter allowing only electrons with an energy above the set threshold to pass through. One condition for such a filter is to have an extremely high vacuum to avoid scattering of electrons on residual gas molecules. The MAC-E filter consists of two superconducting solenoids, which produce a guiding magnetic field. The electrons, originating at the WGTS, are guided magnetically around the magnetic field lines in a cyclotron motion. In the center of the two magnets this field drops by many orders of magnitude, causing the transversal energy to be transformed into mostly longitudinal energy. This works due to the non-relativistic approximation that the magnetic moment of the electrons is conserved [30]:

$$\mu = \frac{E_{\text{trans}}}{B} = \text{const.} \quad (3.5)$$

Here, E_{trans} is the transverse energy of the electrons and B is the magnetic field strength. [30] This leads to

$$\mu_i = \mu_f \quad (3.6)$$

$$\frac{E_i \sin^2(\theta_i)}{B_i} = \frac{E_f \sin^2(\theta_f)}{B_f}$$

with (i) being the initial and (f) being the final state while using $E_{\text{trans}} = E \sin^2(\theta)$ [39]. Here, E is the total energy of the electron and θ is its pitch angle. This results in the following relation for the angle under the assumption of constant energy [39]:

$$\theta_f = \arcsin\left(\sin(\theta_i) \sqrt{\frac{B_f}{B_i}}\right) \quad (3.7)$$

In this case, θ_i is the pitch angle of the electron momentum with respect to the magnetic field direction in the source, θ_f is the pitch angle after the magnetic field has been changed, B_i is the magnetic field strength in the source and B_f is the magnetic field strength after the change [39]. Therefore, the energy resolution of such a filter can be calculated using the following equation

$$\Delta E = E \cdot \frac{B_{\text{min}}}{B_{\text{max}}} \quad , \quad (3.8)$$

with B_{min} being the minimum magnetic field at the analysing plane and B_{max} being the maximal magnetic field in the beamline located at the pinch magnet with $B_{\text{max}} = B_{\text{pch}} = 4.2 \text{ T}$. Both are shown in 3.6 [30]. This shows that the energy resolution is optimal if the magnetic field at the analysing plane is very low compared to the source magnetic field. However, this is proportional to the cross section area A of the flux tube:

$$\Phi = \int B \cdot dA \quad , \quad (3.9)$$

due to the conservation of the magnetic flux Φ . [30]

Pre-Spectrometer

The Pre-Spectrometer (PS) is the first of the two spectrometers in the KATRIN beamline and it was originally designed as a prototype for the MS [30]. The PS is inherently limited by its inner diameter of 1.68 m in terms of its energy resolution and so its mostly used as a pre-filter to reduce the number of electrons that reach the MS. A problem that was noticed about the setup of the PS before the MS is that β -electrons can get trapped in the low potential region between these two. These electrons can accumulate over time and can cause an additional background signal. Thus, the PS is not being used during β scan campaigns [40]. [30]

Another way to boost the energy resolution of the spectrometer is to reflect electrons with large initial pitch angles, since they exhibit the largest remaining transverse energy when maximally aligned in the analysing plane. To achieve the reflection of these electrons, the magnetic mirror effect is employed which is caused by electrons that travel from a low

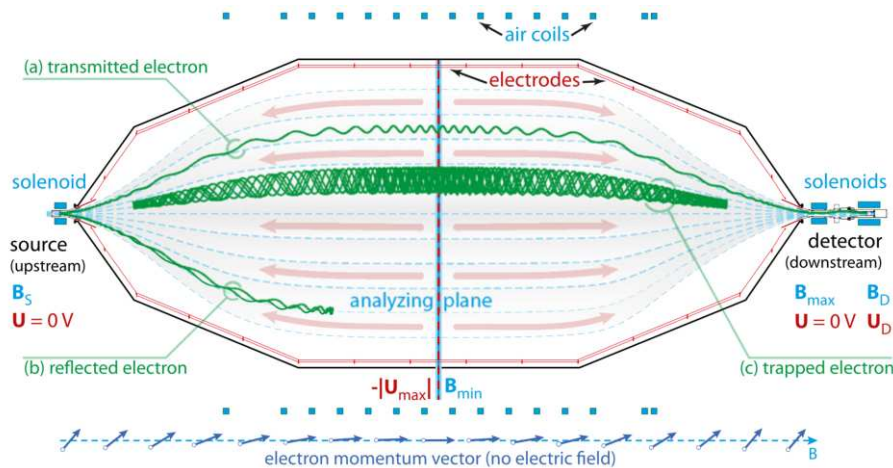


Figure 3.6.: Principle of the MAC-E filter. Electrons are guided through a decreasing magnetic field which converts their transverse energy to longitudinal energy. The field is created by two superconducting solenoids at the ends, as well as an array of so-called air coils around the spectrometer vessel. (a) Electrons are transmitted to detector if their energy is above the retarding potential $|U_{\max}|$. (b) Electrons are reflected back if their energy is below the retarding potential. (c) Electrons which originate from inside of the spectrometer are being reflected and remain trapped due to the magnetic mirror effect. Adapted from [35]

magnetic field to a high magnetic field region. In this case, the electrons are reflected back if the change in magnetic field cause a final angle of $\theta_f \geq 90^\circ$. In KATRIN, as previously mentioned, the highest magnetic field is located at the so-called pinch magnet at the downstream end of the Main Spectrometer. Since the electrons start in the source at a field of $B_{\text{src}} = 2.52 \text{ T}$, this leads to a maximum acceptance angle of 51%. [30]

Main Spectrometer

The Main Spectrometer (MS) is the second of the two spectrometers in the KATRIN beamline and has a diameter far larger than the PS of 10 m and a length of 23.3 m. It uses the same principle of MAC-E filtering as the PS but due to its diameter it has a significantly higher energy resolution. Therefore, with the PS turned off it is the main way to measure the energy of the β -electrons. However, it is also one of the main contributors of the background in the experiment due to various different effects which are further discussed in [39]. [30]

3.2.4. Detector System

After passing the Main Spectrometer the electrons are able to reach the Detector Section where they are detected by the Focal Plane Detector (FPD) which is a silicon p-i-n-diode array with 148 pixels on a diameter of 125 mm and a sensitive area of 90 mm [41]. Each of these pixels works separately, and their signals are read out using amplifiers before the signals are digitized and analyzed using digital filters in a custom DAQ system. Each pixel occupies the same area of 44 mm^2 in the FPD. Due to the detector's poor energy resolution of about 2.2 keV on average for all pixel [42], the MS is used to filter out electrons which

are not in the desired energy range. By varying the retarding potential at the MS, the energy of the electrons can be scanned, and an integral spectrum can be measured. A Post Acceleration Electrode (PAE) is used to accelerate the electrons before they impinge on the detector. This reduces the energy loss in the detectors dead layer and reduced the chance for backscattering at the FPD due to a lower pitch angle. Furthermore, the desired energy range is shifted due to higher energies outside of low background regions. [35, 41]

3.3. Setup for keV-scale Sterile Neutrino Search

For the keV-scale sterile neutrinos search, the KATRIN setup has to be modified in several ways due to several limitations of the current setup. These changes will be discussed in the following sections.

3.3.1. Rear Wall Modification

The first change to the KATRIN setup is the replacement of the RW. The current RW is a gold-coated steel disk with a diameter of 145 mm. However, because of the high atomic charge of gold, it is not ideal for the keV-scale sterile neutrino search. This is due to the high backscattering probability of electrons on gold of possibly over 50% depending on the incident energy and angle, and the resulting energy loss of those electrons[25]. In the current neutrino mass measurement those scattered electrons are so far neglected, because the vast majority of backscattered electrons loses so much energy that they are unable to pass the retarding potential of the MS. However, for the search of keV-scale sterile neutrinos the retarding potential has to be reduced to allow a deep tritium beta decay spectrum scan in search of a kink in the spectrum. Therefore, these electrons from the RW would significantly distort the energy spectrum and impair the measurement. To avoid this, alternative RW materials are currently being researched and tested. Some of the possible candidates are a RW made of beryllium and a RW with a micro-structured surface which is researched in this thesis. Both offer different benefits and drawbacks, which are further discussed in chapter 4.

3.3.2. Field Adjustments

In addition to the RW material, the field configuration of the KATRIN setup has to be adjusted to improve the sensitivity of the sterile neutrino search. One of these changes includes the upgrade of the post-acceleration electrode (PAE) which is used to accelerate electrons towards the detector. This mitigates a multitude of detector systematics such as dead layer energy loss, backscattering, charge sharing between neighboring pixels, as well as signal pileup. [43]

Apart from the PAE voltage, there are several planned adjustments for the magnetic fields. These adjustments are currently being discussed within the collaboration and they will be outlined in the upcoming TRISTAN Technical Design Report. These adjustments target adiabatic transport through the MS, detector backscattering, and the reduction of electrons from RW backscattering in the measured spectrum. The adjustments concerning the latter are summarized in Section 4.2.1.

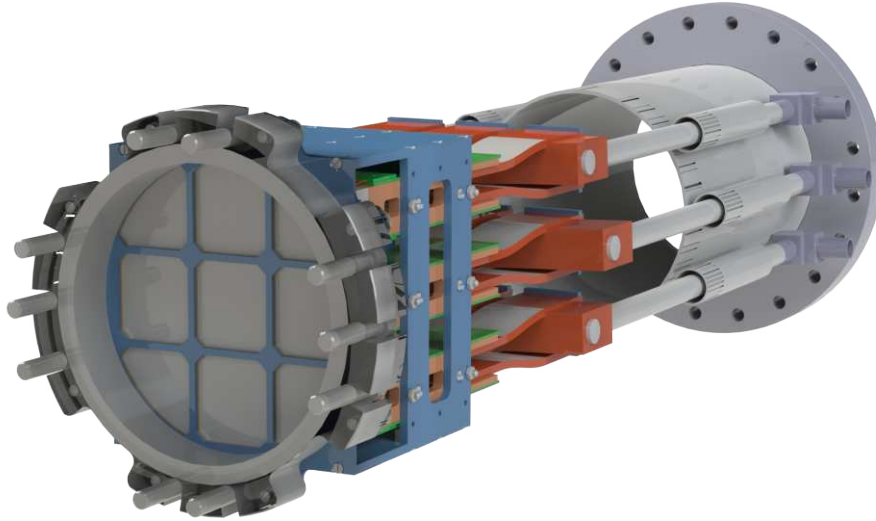


Figure 3.7.: Schematic of the TRISTAN Phase-1 detector from a side view. The detector consists of 9 modules with 166 pixels each, which are held together by a steel structure (light blue). This includes a vacuum aperture. The modules are thermally coupled to a cooling structure. Adapted from [25]

3.3.3. Detector System

The last big change to the KATRIN beamline is the replacement of the Focal Plane Detector (FPD) with a new detector system. This new detector system, which was briefly mentioned in the previous chapter, is the TRISTAN detector. This Silicon Drift detector has to be able to handle the high rate of electrons which are expected in the deep tritium spectrum measurement. Therefore, the detector has to be segmented into 9 modules with 166 pixels of a diameter of 3 mm each. Every pixel is a separate Silicon Drift Detector (SDD) that creates electron-hole pairs when an ionizing particle deposits energy in the detector. These pairs are drifted to the corresponding contacts by the depletion field where they produce a measurable charge signal with an amplitude determined by the deposited energy. The key behind this is the low capacitance due to the drift field which allows the use of point-like anodes much smaller than the pixel size. This results in a larger signal amplitude and shorter rise time. [3]

A schematic of the Phase-1 TRISTAN detector with all nine modules is shown in figure 3.7.

4. RW Scenarios to reduce Backscattering

As previously discussed, one of the largest systematic effects for the keV-scale sterile neutrino search at KATRIN is the backscattering of electrons from the RW. In this chapter, we will first discuss the theoretical basics of electron scattering in section 4.1. Then, we will discuss possible modifications to the RW to reduce backscattering in section 4.2.

4.1. Theoretical Basics of Backscattering

The backscattering of electrons from the RW is a complex process that depends on the total energy as well as the angle of the electrons. It is important to understand the mechanism of electron-nuclei interactions.

4.1.1. Elastic Scattering

The first type of scattering is elastic scattering. In this case, the energy and momentum of the system are unchanged in the process. With the use of four-momentum vectors, one can calculate the differential cross section for elastic scattering. This is done under the assumption that the electron is relativistic and the nucleus is at rest. Using this assumption, the energy of the electron after scattering can be calculated as [10]

$$E' = \frac{E}{1 + \frac{E}{M}(1 - \cos(\theta))}, \quad (4.1)$$

where E is the energy of the electron before scattering, E' is the total energy of the electron after scattering, M is the mass of the nucleus and θ is the scattering angle whose definition is shown in figure 4.1. Depending on the mass number A of the nucleus and energy of the electron, this can vary significantly for forward and backward scattering, which is shown in figure 4.3. The equation further implies that the elastic scattering energy loss is fully correlated with the scattering angle. [10]

To fully describe the kinematics of the process one must also calculate the differential cross section, which determines the probability for each scattering angle. The basic way to do this is to use the so-called Rutherford cross section. For this, it is necessary to neglect spin effects for now and assume that the electron is non-relativistic. In addition, if the nuclei

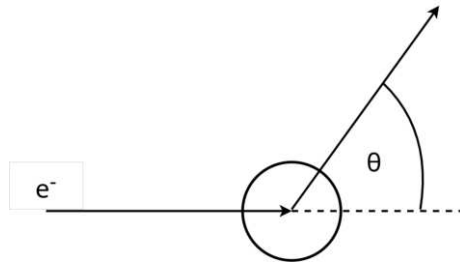


Figure 4.1.: Definition of the scattering angle θ for elastic scattering.

are sufficiently heavy compared to the electron mass, the recoil energy can be neglected. With these assumptions, the Rutherford cross-section can be calculated as [10]:

$$\left(\frac{d\sigma}{d\Omega}\right)_{\text{Rutherford}} = \frac{(zZe^2)^2}{(4\pi\epsilon_0)^2 \cdot (4E_{\text{kin}})^2 \sin^4(\theta/2)} \quad (4.2)$$

where z is the charge of the incoming particle, an electron in this case, Z is the charge of the nucleus, e is the elementary charge, ϵ_0 is the vacuum permittivity and E_{kin} is the kinetic energy of the electron. This equation holds for the case where the electron is farther away from the scattering center than the radius of the said center.

However, the Rutherford cross section is only valid if the spin of both scattering partners is neglected and the particle is non-relativistic. If the particle is assumed to have relativistic energies and the spin is taken into account, the cross section has to be modified. This is done by the so called Mott cross-section which is given by [10]:

$$\left(\frac{d\sigma}{d\Omega}\right)_{\text{Mott}} = \left(\frac{d\sigma}{d\Omega}\right)_{\text{Rutherford}} \cdot \left(1 - \beta^2 \sin^2 \frac{\theta}{2}\right), \quad \text{with } \beta = \frac{v}{c} \quad (4.3)$$

The helicity conservation for particles which move with the speed of light, which was previously explained, is visible in the additional factor added to the Rutherford cross-section. This has to be considered in the KATRIN experiment with a maximum value of $\beta \approx 0.26$.

The Mott cross section is a good approximation for the differential cross-section of elastic scattering for electrons with relativistic energies, but it only holds for the case of a momentum transfer $|\mathbf{q}|$ of close to zero. For $|\mathbf{q}| \neq 0$, one has to consider the spatial extension of the nucleus because the particle only sees a partial charge. This is taken into account using the form factor $F(q^2)$. This form factor has to be determined experimentally by measuring the difference between the Mott cross-section and the measured cross-section[10]:

$$\left(\frac{d\sigma}{d\Omega}\right)_{\text{exp}} = \left(\frac{d\sigma}{d\Omega}\right)_{\text{Mott}} \cdot |F(q^2)|^2 \quad (4.4)$$

The electron beam for this typically originates from accelerators and the measurement has to be repeated for all angles.

If the recoil is negligible and if the Born approximation holds, the form factor can be calculated as the Fourier transform of the charge distribution $\rho(\mathbf{x})$ of the nucleus. So, the

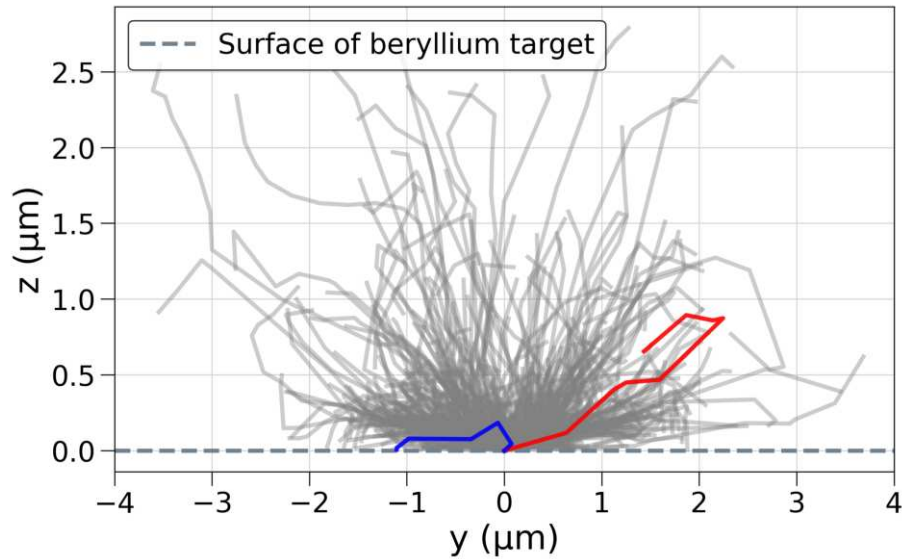


Figure 4.2.: Multiple scattering processes inside of a beryllium target. Red shows an electron terminating inside of the beryllium while blue shows an electron being backscattered after multiple scatterings inside the beryllium.

Table 4.1.: Form factors for different charge distributions. Adapted from [10]

charge distribution		$F(q^2)$	
Point	$\frac{\delta(r)}{4\pi}$	1	constant
Exponential	$\frac{a^3}{8\pi}e^{-ar}$	$(1 + q^2/a^2\hbar^2)^{-2}$	Dipole
Gaussian	$(a^2/2\pi)^{3/2}e^{-a^2r^2/2}$	$e^{-q^2/2a^2\hbar^2}$	Gaussian
Homogenous sphere	$\begin{cases} 3/4\pi R^3 & \text{for } r \leq R \\ 0 & \text{for } r > R \end{cases}$	$3/4\pi 3\alpha^{-3}(\sin \alpha - \alpha \cos \alpha)$ with $\alpha = \mathbf{q} R/\hbar$	oscillating

form factor is given by [10]:

$$F(q^2) = \int \rho(\mathbf{r})e^{i\mathbf{q}\cdot\mathbf{x}}d^3x \quad (4.5)$$

For a spherically symmetric charge distribution this can be calculated relatively easily. However, the exact charge distribution one has to use depends on the nucleus in question. Some examples are shown in figure 4.1. In general, one can say that most nuclei have a homogeneous charge distribution with a rather sharp edge which corresponds to an oscillating form factor. In spite of that, in the case of the new KATRIN RW material, beryllium is investigated as a candidate which is one of these exceptions with a more gaussian-shaped charge distribution [10].

4.1.2. Inelastic Scattering

All of the previous calculations are done under the assumption that the electron scatters elastically, but there are also inelastic scattering processes that can occur. In the case of such scattering events, the ingoing and outgoing particles can be different, so the total momentum due to excitation of the target nucleus is not conserved. This can be seen in a spectrum as high peaks at positions of nuclear energy levels. [10]

The excitation of such nuclei can occur in several ways. One is the excitation of inner-

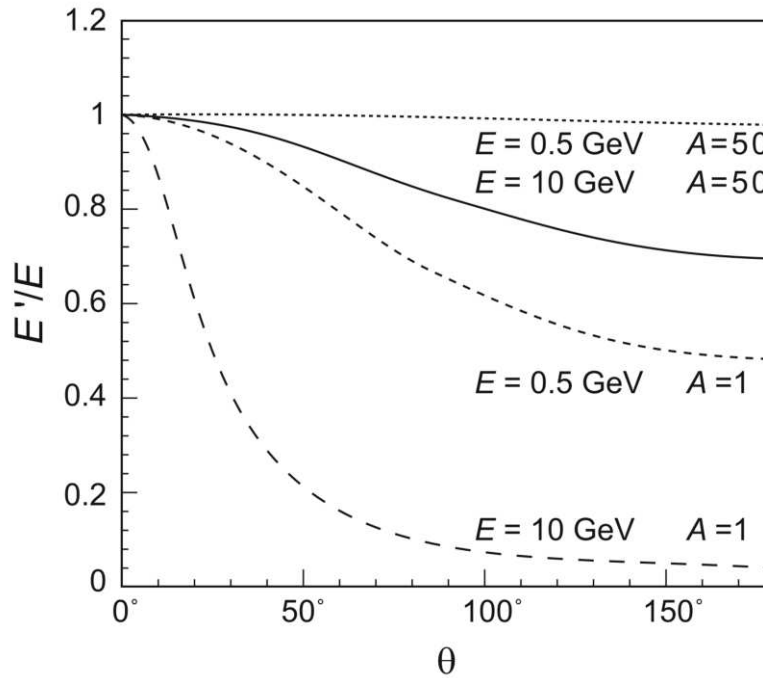


Figure 4.3.: Energy of the electron after elastic scattering as a function of the scattering angle for different mass numbers A of the nucleus. However, this effect is on the order of $< 10^{-3}$ % for the low keV scale. Adopted from [10]

shell electrons. For such a process the incident electron requires high energy to excite an electron on the lower shells to unoccupied ones in the shells above the Fermi level. This leaves the atom in an excited state, whose de-excitation can be accomplished by emitting X-ray photons or by the emission of another electron that are called Auger electrons. The Auger effect occurs, because of electrons that fill a inner-shell vacancy, producing energy, which in turn causes the emission of an electron from a different shell. Another way of excitation due to an incidence electron is the excitation of outer-shell electrons. This can also cause the emission of secondary electrons given high enough energy with emission of visible electromagnetic radiation or generation of heat in the following de-excitation process. [44]

The range of these incident electrons can be calculated in multiple ways. One of the well-known ways of achieving this is the so called Bethe-Bloch formula. It uses the atomic number of the target and the kinetic energy of the incident electron to calculate the range for high-energy electrons [44]:

$$-\frac{dE}{dz} = \frac{2\pi e^4 N Z}{E} \ln \left(\frac{1.166E}{I} \right) \quad (4.6)$$

Here, N is the number of atoms per unit volume, Z is the atomic number of the target, E is the kinetic energy of the incident electron, and I is the mean excitation potential. Looking at this equation, it becomes clear that it results in negative results for $E < I/1.166$, which is not physically possible. However, in the case of beryllium the threshold is 54.63 eV according to data from [45]. This makes it applicable for the energy range that is being researched in this thesis. [44]

4.1.3. Backscattering Coefficient

The backscattering coefficient η_{BS} is defined as the fraction of of the incident beam which return after scattering. In measurements, this takes into account the electrons with an energy above 50 eV due to low energy secondaries. This assumption is valid due to the low and therefore, negligible amount of secondary electrons compared to the number of primaries above this energy region. There are multiple semi-empirical models that describe this coefficient with differing energy and atomic charge ranges. [44]

One such model is the Everhart Model, which applies to electrons with an energy above 10 keV and an atomic number of the target nucleus below ~ 45 . The Everhart Model is based on the assumption of Thomson-Whiddington for the energy loss [44]:

$$E_0^2 - E^2 = cz \quad (4.7)$$

Here, E_0 is the initial electron energy, E is the most probable energy at a depth of z in the material and c is a target dependent constant. This assumption yields after some calculations the following equation for the backscattering coefficient [46]:

$$\eta_{BS} = \frac{a - 1 + 0.5^a}{a + 1} \quad \text{with } a = \frac{\pi Z^2 e^4 N_A}{m_e^2 c A} \quad (4.8)$$

Here, Z is the atomic number, A is the gram atomic mass of the target material, e is the electron charge, and m_e is the electron mass. At last, $N_A = 6.023 \times 10^{23}$ atoms/mole is the Avogadro's number and c is the same constant as in the equation (4.7). The complete derivation can be found in [46].

The equation (4.8) implies an almost linear increase with Z due to Z/A being close to constant for most elements. Therefore the accepted value for a with the highest agreement with experimental data is $a = 0.045Z$ [44]. In addition, there is no explicit primary electron energy dependence, which could explain the limit of the models precision below 10 keV.

4.2. Possible RW Modifications

We will now discuss possible modifications to the RW and rear section of the KATRIN experiment to decrease the amount of backscattering electrons that reach the detector system.

4.2.1. Magnetic Field Adjustments

One of the possible ways to reduce the number of RW backscattering electrons in the measured spectrum is to adjust the current magnetic field configuration. This is due to the magnetic mirror effect explained in section 3.2.3. There are three important ways to achieve this which will be discussed in the following.

Increasing Source Field

The first optimization is to guide as many electrons as possible directly to the detector instead of reflecting a large portion at the maximal magnetic field downstream B_{md} . For this reason, it is best to have $B_{\text{md}} \approx B_{\text{src}}$ [47]. To achieve this, one can decrease B_{md} and increase B_{src} (the maximum for B_{src} is the design value of 3.6 T [48]). Having both fields at a high value is preferred for optimal magnetic trapping of RW backscattering electrons (see next paragraph).

Another benefit is the increased difference between source and RW field, which would lead to a magnetic trap for some of the backscattered electrons and therefore a higher number of scatterings at the RW possibly leading to absorption. [47]

Decreasing RW Field

The second optimization is to improve the magnetic trapping of backscattered electrons from the RW. This can be achieved by decreasing the magnetic field at the RW, which leads to more backscattered electrons being magnetically reflected by $B_{\text{src}}/B_{\text{md}}$, giving these electrons another chance to be absorbed by the RW. This goes hand in hand with the previous point as the difference between the source and RW field is increased. As previously discussed, such a magnetic trap depends on the pitch angle of the electron and the magnetic field configuration. However, a lower magnetic field at the RW would also require a larger RW due to magnetic flux conservation which would likely require a redesign of the rear section of the experiment. However, it is possible to decrease the RW field and the detector field by the same factor, which guarantees that the flux tube size remains constant ($B_{\text{det}} \cdot A_{\text{det}} = B_{\text{rw}} \cdot A_{\text{rw}}$). The lower limit for B_{rw} is then determined by the minimally acceptable detector magnetic field. [47]

More information on possible magnetic field adjustments and more drastic changes can be found in [47].

4.2.2. Electric Field Adjustments

Another way to reduce the detected backscattered electrons is to change the electric field at the RW in addition to the magnetic field. This would have the benefit of not changing the magnetic field configuration and thus not affecting the flux tube transmission. In addition, the electric field allows for a more direct control of the backscattered electrons.

Blocking Potential

The first possibility to discuss is the use of a negative electric blocking potential in between the RW and the WGTS, e.g. by using a ring electrode. With a potential barrier larger than the tritium endpoint energy ($|U| > 18.6 \text{ keV}$) it would reduce the RW contribution to practically zero.

However, this comes with the downside that tritium decays occur within the potential creating a non-trivial second spectrum due to electrons with different energies being created at varying starting potentials [47]. Another downside to this approach is the trapping of

electrons between the blocking potential and the MS potential which would require another way to remove these electrons, e.g. by using a wiper wire or a drift field. [47]

Absorbing Potential

A second possibility is to set a positive voltage on the RW itself. This would accelerate electrons moving towards the RW and significantly help to contain electrons coming back from the RW and significantly help to contain electrons coming back from the RW. However, very high voltages would be necessary to completely absorb all electrons which could prove to be challenging due to the strong magnetic field, potential sparking because of insufficient insulation and space. Therefore, high voltages may not be feasible and a compromise would be necessary. This could be a voltage where all secondary electrons originating Auger or X-ray processes are absorbed, which could already reduce systematics significantly and ease spectrum modeling. Alternatively, the MS potential could be set sufficiently high to block all RW secondaries at the cost of decreasing the measured energy range. [47]

Both of these possibilities are currently still part of an ongoing research but could be a promising way to reduce the background in the KATRIN experiment. However, the absorbing potential would not require a potential as high as the blocking potential and could therefore be easier to implement while still offering significant benefits in terms of systematics mitigation, but further research is necessary to understand all effects of these changes on the experiment.[47]

4.2.3. Rear Wall Material

We will now discuss the possibility of changing the material of the RW itself. Currently, the RW is made of a gold coated stainless steel disk. However, gold has a high atomic number Z and therefore a high backscattering probability of 48.1% [25]. This can be mitigated by using a material with a lower atomic number, which would significantly reduce the backscattering probability, which is approximately proportional to $\eta_{BS} \propto Z$ if $Z/A \approx \text{const.}$ as discussed in section 4.1. Therefore, by using a material like beryllium ($Z = 4$) the backscattering probability could be reduced without further adjustments due to its low backscattering probability which is shown in figure 4.4. However, beryllium also poses several challenges. First, it is a toxic material that is harmful to humans and the environment if no proper care is taken during the production and handling of the material. Secondly, it is currently unclear how the material would interact with the tritium gas in the rear section of the experiment and if it is more prone to adsorbing tritium than gold. However, preliminary measurements indicate that beryllium does not accumulate more tritium on its surface than gold [49]. Thirdly, it has to be tested whether beryllium can be decontaminated using ozone (see [34]) without growing an oxide layer on the surface. Therefore, other candidates are also being considered, such as silicon ($Z = 14$) which is better understood by the KATRIN group and less toxic than beryllium.

In addition, the RW could also charge up due to charge carriers such as electrons in case the material is non-conductive, as is the case for most metal or semiconductor oxides.

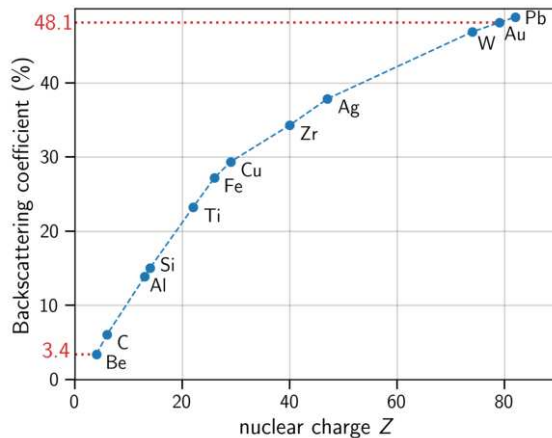


Figure 4.4.: Backscattering probability as a function of the nuclear charge Z of the RW material determined using Geant4 simulations for electrons shot at a target with an energy of 18.5 keV at an angle of 0° . Adopted from [25]

Therefore, there would be an electric field at the RW which is time-dependent and could lead to additional systematic effects.

4.2.4. Micro-structured Rear Wall

The idea of a micro-structured RW was taken from the passive Transverse Energy Filter pTEF which was used in the KATRIN experiment to determine the angle distribution of the electrons at the detector [39]. The pTEF is a gold coated hexagonal grid, as shown in figure 4.5 that is placed in front of the detector. Due to the magnetic field in the experiment, electrons would move on a helical path with a radius defined by the magnetic field strength, the angle, and the energy of the electrons. During this motion, the particles would hit the wall and scatter inside the channels of the grid, losing energy in the process. This way, a majority of these β -electrons would not be able to reach the detector while the background would be able to pass through with less complications due to their lower pitch angle. More information on pTEF can be found in [39]. The idea of a micro-structured RW goes is very similar to placing a pTEF in front of the RW. In the case of a micro-structured RW, the RW is exchanged with a new one. In the case of the pTEF, a micro-structured grid is placed in front of the RW. This could be done without changing anything about the RW. In both cases, the scattering inside of the channels causes the electrons to lose energy, which prevents them from reaching the detector. However, a direct comparison between the two has shown that they are very similar in their effectiveness in reducing the backscattering on the RW, but the pTEF in front of the RW would cause a larger surface increase where tritium could be adsorbed. The results of these simulations and how the comparison is made are discussed in Chapter 6

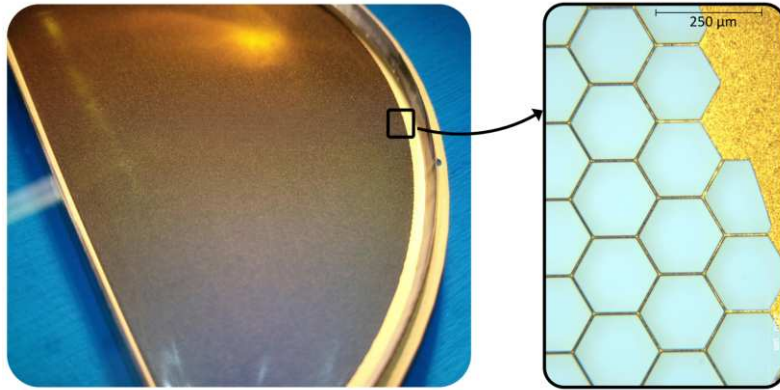


Figure 4.5.: Photo and optical microcope image of the pTEF, that was used as background filter at the detector. Adopted from [39]

5. Modeling of the RW and Beamline

5.1. Basics of Geant4 based Simulations

Geant4 (GEometry ANd Tracking) is a C++ based software toolkit that has been developed at CERN. It is designed to simulate interactions of particles while they traverse matter. Its applications are immense, as it finds a use in high-energy physics, astrophysics, medical physics, and even radiation safety. The toolkit offers a broad set of tools for the simulation particle interactions in matter, in particular for particle tracking, the modeling of physical processes, and the description of detector geometries of arbitrary complexity. This section gives an overview of the main concepts and components of Geant4 that are pertinent to scientific simulations. The basics regarding the initial setup and minimal architectural features to be fulfilled for developing a simulation are also covered. All information in this section is based on the official Geant4 Application Developer Guide [50].

5.1.1. Architecture and Core Concepts

Geant4 is designed with a modular architecture, allowing for high flexibility and customization. At its core, the framework consists of several key components, each of which can be tailored to the specific needs of the simulation. The primary components are:

- **Detector Construction:** One essential aspect of a Geant4 simulation is the definition of the geometry. Geometry, in this context, refers to the physical arrangement of materials and detector components with which the particles will interact. Geometries are defined through a hierarchy of volumes, consisting of solids (shapes), logical volumes (defining materials and properties), and physical volumes (placement within the simulation). This hierarchy allows for complex detector geometries to be constructed, with repeated structures or nested volumes handled through instantiation.

The materials in Geant4 are described by their elemental composition, density, and other physical properties. These materials are assigned volumes to accurately model their interaction with particles. The precision of the geometry definition is essential, as even minor inaccuracies in material properties or placement can affect the accuracy of the simulation results.

- **Particle Tracking:** Particle tracking in Geant4 refers to the simulation of a particle's motion through the defined geometry, taking into account all relevant physical processes that may affect its trajectory. Geant4 follows a stepwise approach, breaking the particle's path into small segments (steps) where interactions with the surrounding material can occur. The tracking system ensures that particles are correctly transported through boundaries between different volumes, and materials and that they are subject to the physical processes active within each region.

The accuracy of the tracking is crucial, particularly in high-energy physics experiments, where precise modeling of particle interactions with detector components is required. Geant4 supports various coordinate systems, and its flexible framework allows the integration of custom tracking algorithms if necessary.

5.1.2. Physics Processes

Geant4 provides a wide range of physics models to simulate the interactions of particles with matter. These processes span electromagnetic, hadronic, and optical interactions as well as radioactive decay and the transport of ions. Each physics process is implemented using a modular approach, allowing users to select and configure the processes most relevant to their specific application.

- **Electromagnetic Processes:** The electromagnetic processes in Geant4 cover a wide range of interactions, including ionization, Bremsstrahlung, Compton scattering, and pair production. The toolkit provides standard and low-energy electromagnetic models, which can be chosen depending on the energy range of interest. The low-energy models are particularly useful for medical physics applications, where an accurate simulation of interactions at energies below 1 MeV is essential.
- **Hadronic Processes:** For hadronic interactions, Geant4 includes several models that cover elastic and inelastic scattering, as well as nuclear interactions. The toolkit supports different modeling approaches, such as parameterized models (based on experimental data), and theoretical models (based on quantum chromodynamics or phenomenological approximations). The choice of hadronic models depends on the specific type of simulation that is performed, with high-energy experiments often requiring precise modeling of hadron-nucleus interactions.
- **Optical Processes and Radioactive Decay:** Geant4 also supports optical processes, including scintillation and Cherenkov radiation, which are crucial for the simulation of many detector systems. Additionally, Geant4 has an integrated framework for simulating radioactive decay, allowing modeling of decay chains, energy spectra, and time-dependent phenomena.

5.1.3. Basic Setup and minimal Architecture

A Geant4 simulation requires the implementation of several core classes, each corresponding to a specific part of the simulation process. At a minimum, the following components must be defined to create a functional simulation.

Main Program (Main Function)

Every Geant4 application begins with a main function that initializes the run manager, which controls the flow of the simulation. This is where the core Geant4 components, such as geometry, physics lists, and particle sources, are instantiated and managed.

```
int main(int argc, char** argv)
{
    G4RunManager* runManager = new G4RunManager;
    runManager->SetUserInitialization(new DetectorConstruction);
    runManager->SetUserInitialization(new PhysicsList);
    runManager->SetUserAction(new PrimaryGeneratorAction);
    runManager->Initialize();
    runManager->BeamOn(numberOfEvents);
    delete runManager;
    return 0;
}
```

Detector Construction

The DetectorConstruction class is responsible for defining the geometry and materials of the simulation. This involves creating solids (shapes), assigning materials to logical volumes, and placing these volumes in the world volume, which represents the simulation space.

```
G4VPhysicalVolume* DetectorConstruction::Construct()
{
    G4Box* worldBox = new G4Box("World", // Name
                               1.0*m, 1.0*m, 1.0*m); // x, y, z
    G4Material* air = nistManager->FindOrBuildMaterial("G4_AIR");
    G4LogicalVolume* worldLog = new G4LogicalVolume(worldBox, // solid
                                                    air, // Material
                                                    "World"); // Name
    G4VPhysicalVolume* worldPhys = new G4PVPlacement(0,
                                                    G4ThreeVector(),
                                                    worldLog,
                                                    "World",
                                                    0, false, 0);

    return worldPhys;
}
```

Physics List

The PhysicsList class defines the physical processes that govern the interaction of particles with matter in the simulation. Geant4 provides pre-built physics lists for common applications, but users can also create custom physics lists by combining individual processes.

```
void PhysicsList::ConstructProcess()
{
    G4EmStandardPhysics* emPhysics = new G4EmStandardPhysics();
    RegisterPhysics(emPhysics);
    // Additional physics processes can be registered here
}
```

Primary Generator Action

The PrimaryGeneratorAction class specifies the initial conditions of the particles to be tracked in the simulation. This includes particle type, energy, position, and direction. Geant4 provides several built-in options for generating primary particles, such as the General Particle Source (GPS).

```
void PrimaryGeneratorAction::GeneratePrimaries(G4Event* anEvent)
{
    G4ParticleGun* particleGun = new G4ParticleGun(1);
    G4ParticleDefinition* particle =
    G4ParticleTable::GetParticleTable()->FindParticle("geantino");
    particleGun->SetParticleDefinition(particle);
    particleGun->SetParticleEnergy(1.0*GeV);
    particleGun->GeneratePrimaryVertex(anEvent);
}
```

Run and Event Actions

The simulation is controlled by the G4RunManager, which handles the initialization of the simulation and manages the event loop. Each event corresponds to the interaction of a primary particle with the detector geometry and its associated physics processes. The results of each event can be processed through sensitive detectors, where information about energy deposition, track lengths, and other quantities can be recorded.

The minimum requirements to run a Geant4 simulation are the implementation of the classes mentioned above. A strength of Geant4 is its flexibility, allowing users to customize and extend the simulation framework to suit their specific needs. This includes the ability to define custom geometries, physics processes, and user actions, as well as incorporate external libraries and tools. This modular design is the reason for its wide use in scientific applications.

5.2. Micro-structured Rear Wall Implementation

For the simulation of the micro-structured RW, a Geant4 application was developed to model the interaction of electrons with the geometry of the RW. Here, different materials and micro-structures were tested to determine the optimal configuration.

The most important part of the simulation is the definition of the geometry, which includes the RW and the terminator. For this, a construction class was implemented that includes

multiple methods to define the volumes, materials, and electromagnetic fields. The creation of a micro-structure is split into a separate function, which returns a logical volume so that the replacement with different structures is easily implemented. For the creation, a `G4MultiUnion` was used due to the complex structure with several combined `G4Polyhedra` combined to form a single volume. These volumes include a second daughter volume placed inside the RW volume to simulate a variable thickness of the oxide layer. The magnetic fields are also crucial in the simulation of a micro-structured RW due to the cyclotron motion of the electrons, which is necessary for correct results. For this, one important parameter is the magnetic field strength at the RW of 1.26 T. Another important parameter is the `DeltaChord`, which originates from the approximation of the cyclotron motion as a number of straight lines and, therefore, defines the maximum length of a straight line. A correct value should always be in the order of the size of the smallest structure in the simulation. Therefore, the `DeltaChord` was set to 100 nm to ensure a correct simulation of the cyclotron motion of the electrons while saving time.

The next important part is the definition of the custom physics list. Here, multiple different effects must be included to achieve a realistic simulation. The most important is the inclusion of the most suitable electromagnetic physics constructors. There are several options available, but the most suitable for low-energy electrons in the KATRIN experiment are the `G4EmPenelopePhysics` and `G4EmStandardPhysicsSS` constructors. The first is the same as the `G4EmStandardPhysics_option4` with the exception of electrons below 1 GeV which uses specific Penelope models instead. The second is the single-scattering model. This model is known to be the most accurate in most cases and is mostly used for verification purposes. However, this comes with a significant increase in computational cost, which is why the Penelope model is used for the most simulations because it offers a good compromise between accuracy and speed. Another important part is the inclusion of the `G4StepLimiter`, which limits the step size of the particles to a maximum value. This is necessary because of the small oxide layer thickness of only a few nm that would otherwise result in incorrect results due to the too large step size. [51, 52]

The last important part is the definition of the primary generator action. Here, the primary particles, their energy and their angle are defined. In this case, these primary particles are electrons with an energy of up to 18.6 keV and a pitch angle of up to 90°. Assuming that the magnetic field lines are perpendicular to the RW surface, the pitch angle is identical to the polar angle in spherical coordinates (the RW is oriented in the xy-plane and the z-axis is perpendicular to the RW surface). The specific implementation of the generator depends heavily on the specific requirements of the simulation and will therefore be discussed in more detail in the next chapter.

All of these parts interact with each other. For example, the generator class takes the defined geometry into account to automatically adjust the starting position of the electrons and the position of the terminator. In addition, due to the large computational complexity of the simulation, the simulation is written in a way so that parallelization using the `Geant4` multi-threading is possible, which allows the use of multiple CPU cores. In the case of the Tesla cluster at the KATRIN experiment, this allows for 80 CPU cores to be used

simultaneously, which significantly reduces the time needed for the simulation.

All of these Geant4 simulations require a macro file to change the parameters of the simulation during runs without the need for recompilation. Due to the large number of angle and energy combinations, a Python class was written to be used as a wrapper to run the simulations with a given range of parameters and structures. This allows for a large number of parallel and serial simulations without the need for manual intervention.

5.3. Beamline Model

The changes of multiple hardware components in the KATRIN experiment, such as the RW, require a detailed beamline simulation to understand the impact of these changes on the overall performance of the experiment. Therefore, M. Descher et al. have developed a simulation tool called TRModel (see [25]) to simulate the beamline of the KATRIN experiment. TRModel allows sensitivity studies to be performed in a reasonable amount of time, which is crucial for the upcoming start of sterile neutrino measurements in 2026.

This section will give an overview of some of the key features of TRModel and how it is used to simulate the RW modifications investigated in this thesis. Section 5.3.1 will give a brief overview of the architecture, and Section 5.3.2 will go into more detail about the response matrix formalism used in TRModel.

5.3.1. Overview of TRModel

TRModel is a simulation tool to model the beamline of the KATRIN experiment to research the impact of hardware changes on the overall performance of the experiment and estimate the sensitivity for TRISTAN. For this, most critical components and systematic effects are implemented and simulated to find the optimal settings for the experiment. The main features of TRModel include a differential detector response, an increased energy range compared to the neutrino mass measurement, which mainly focused on the endpoint region, and a detailed description of the electron pitch angle distribution. More information on the systematic effects included can be found in [25].

The general structure of the code is divided into several parts that are responsible for different tasks. The main part is the global model that is the main executable of the code. A user can define a set of parameters to define the effects to use for the simulation while either the function `model_differential` or `model_integral` is used to calculate the corresponding energy spectrum. It does so by collecting all necessary responses from the dedicated sub-packages and applying them in the correct order. For the integral model the differential model is applied and evaluated for different retarding potentials and the integral rate at each retarding potential is determined by integrating the differential spectra over a specified energy region of interest. [25]

The sub-packages consist of several categories, which are responsible for different tasks, and in conjunction they are used to form a model of the beamline as a whole. The individual packages can be used by themselves with the exception of the propagation model, which

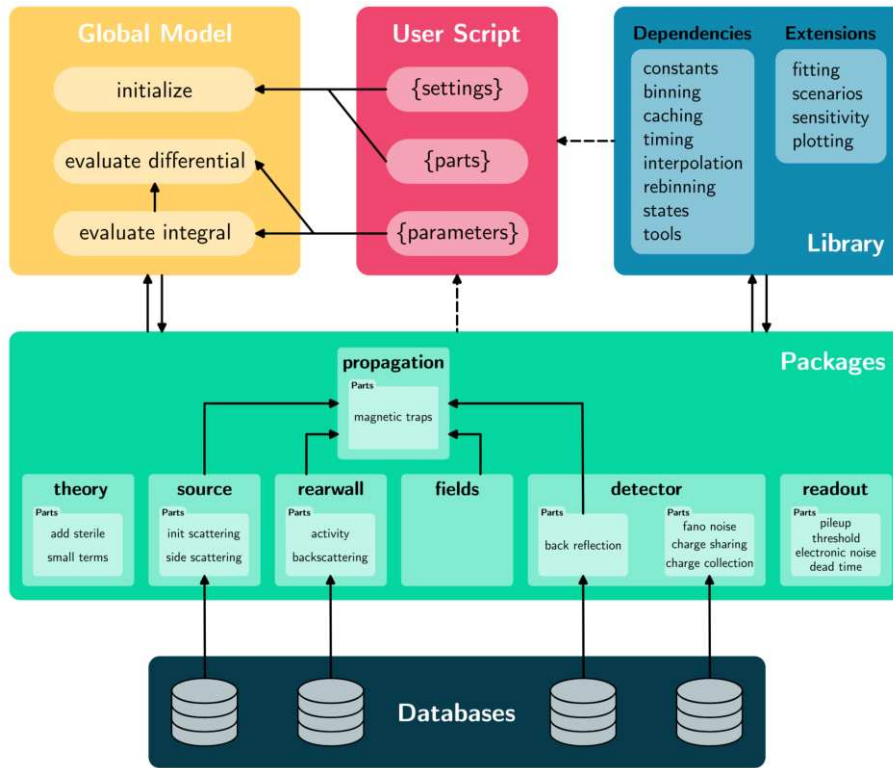


Figure 5.1.: General layout of the TRModel codebase. Adopted from [25]

is essentially an extension of the global model. All sub-packages contain a set of functions to calculate or load their corresponding response matrices and apply them as needed. The general layout of the codebase is shown in figure 5.1. [25]

5.3.2. Response Matrix Formalism

TRModel uses a response matrix formalism to simulate the energy spectrum of the KATRIN experiment. This means that a forward convolution is used to calculate the probability distribution in terms of the electron energy and pitch angle at all relevant locations along of the KATRIN beamline. The electron distribution $S(E, \cos \theta)$ is represented as a 2D matrix by intergrating over the energy-angle bins. The responses are generally, represented by 4D matrices, whose entries specify the probability that a particle from a given angle and energy bin ends up in a different energy or angle bin after passing through a certain component. Thereby, the non-diagonal matrix elements are probabilities for electrons to move from one bin to another. These response matrices are calculated using Monte Carlo simulations and analytical models of the beamline components. This allows fast and precise simulations due to the relatively low computational cost of matrix multiplication with the given multiplication:

$$S_{\text{out}} = R \cdot S_{\text{in}} \quad (5.1)$$

Here, S_{in} is the input spectrum, S_{out} is the output spectrum, and R is the response matrix. However, this causes a loss of information as the energy and angle of the particles are binned into discrete values. This is a trade-off between speed and accuracy, which is necessary for the simulation of the KATRIN experiment. [25]

6. Simulations of a Micro-structured RW

The use of micro-structured surfaces to reduce backscattering has the potential to significantly reduce the background originating from the backscattered electrons at the RW. However, so far the impact of such a modification has not been studied in detail. Therefore, this chapter will focus on the investigation of the impact of such a micro-structured RW on the backscattering and the RW activity. This also includes the comparison of different materials and geometries of the micro-structured RW as well as the impact of the RW modifications on the sensitivity of the KATRIN experiment.

6.1. Backscattering Simulations

6.1.1. Introduction

To simulate the backscattering of electrons at the RW a Geant4 simulation was used, which was developed in the context of this thesis. For improved computational performance, the simulation geometry includes only a small segment of the RW with a size still much larger than the maximum Larmor radius the electrons at the maximum energy of 18.6 keV (see Figure 6.1a). The simulation includes two possible micro-structures, as well as the flat RW which is currently in use. The two micro-structures are the hexagonal pTEF structure (see Section 4.2.4) and an inverted pyramid structure with a height of 600 μm and four equal sides of 100 μm of the base. However, as shown later, the inverted pyramid structure performs worse than the pTEF structure and is therefore not shown in most of the following plots (see Figure 6.5a). All the structures also include an oxide layer with a variable thickness of 0 nm to 10 nm which is expected to be present at the RW for beryllium and silicon. However, the simulation accuracy for such a small layer is hard to judge in Geant4 due to high inaccuracies in the simulation of thin layers [53]. Therefore, future measurements will be necessary to verify the impact of the oxide layer on the backscattering probability.

The RW segment lies in the xy-plane (perpendicular to the z-axis). The electrons are generated a short z-distance away from the central cell of the RW segment. The xy-coordinate is randomly generated within a shape equal to the base cell of the micro-structure (i.e. a hexagon for the pTEF and a square for the pyramid). In the case of

the pTEF, the base cell consists of the inner cell in addition to half of the wall to the neighboring cell. The z-distance to the structure is chosen as 10 μm from the highest z-position of the structure. In this area the electrons are started homogeneously and are directed towards the RW with a specific angle of incidence, which is defined as the angle between the electron's momentum vector and the normal vector of the RW as seen in figure 6.1.

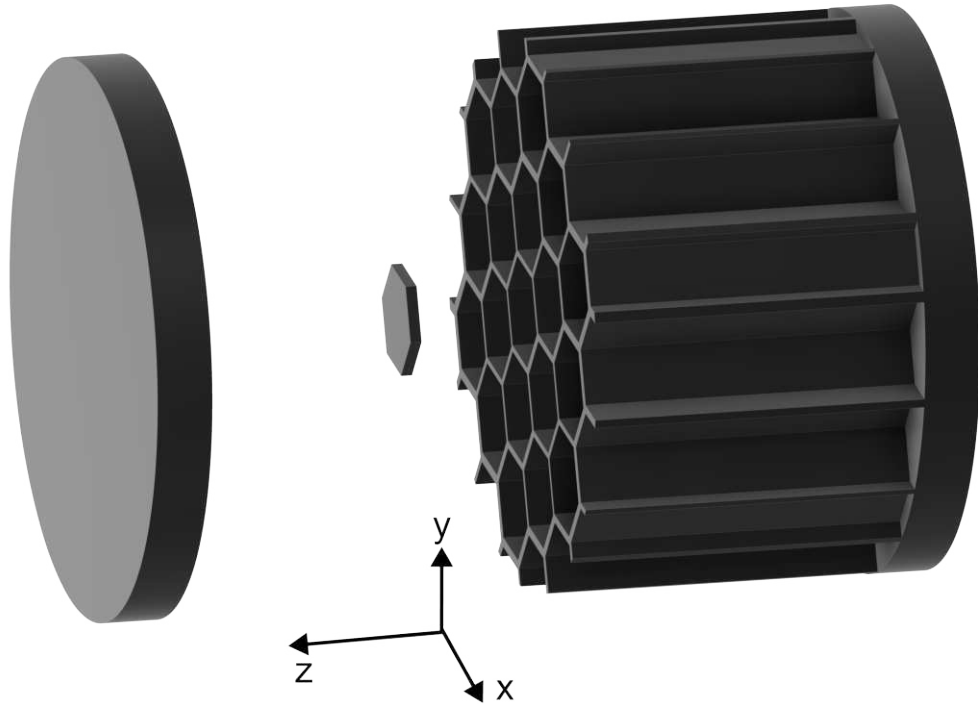
The electrons are then tracked until they lose all their energy or are backscattered, i.e. if they reach the circular terminator in Figure 6.1b. This is done for all angle and energy bin combinations as required for use with TRModel ($E = 100\text{ eV} - 18\,600\text{ eV}$ at 185 eV bin width and $\cos\theta = 0.0 - 1.0$ at 0.04 bin width). Within each bin, E and $\cos\theta$ are drawn from uniform distributions.

The results of these simulations are then used to calculate the backscattering probability for each bin, which is defined as the number of backscattered electrons divided by the number of electrons started in the bin. To keep a balance between the computational cost and high statistics, one million electrons are simulated per bin. In the simulations, there is also a constant magnetic field of 1.26 T to simulate the magnetic field of the KATRIN experiment at the RW. This is done to take into account the Larmor radius of the electrons, which is of no importance in case of a flat RW, but becomes very significant in the simulation of a micro-structured RW. In these simulations, Geant4 version 11.0.3 was used with the SingleScattering physics model, which is the most accurate model for the scattering simulations of electrons in the given energy range according to [54]. However, for early simulations and verification purposes the Penelope physics model was used, which combines a high accuracy with a reasonable computational cost. For this, some additional physics processes were necessary to be activated manually to achieve almost the same results between the two physics models.

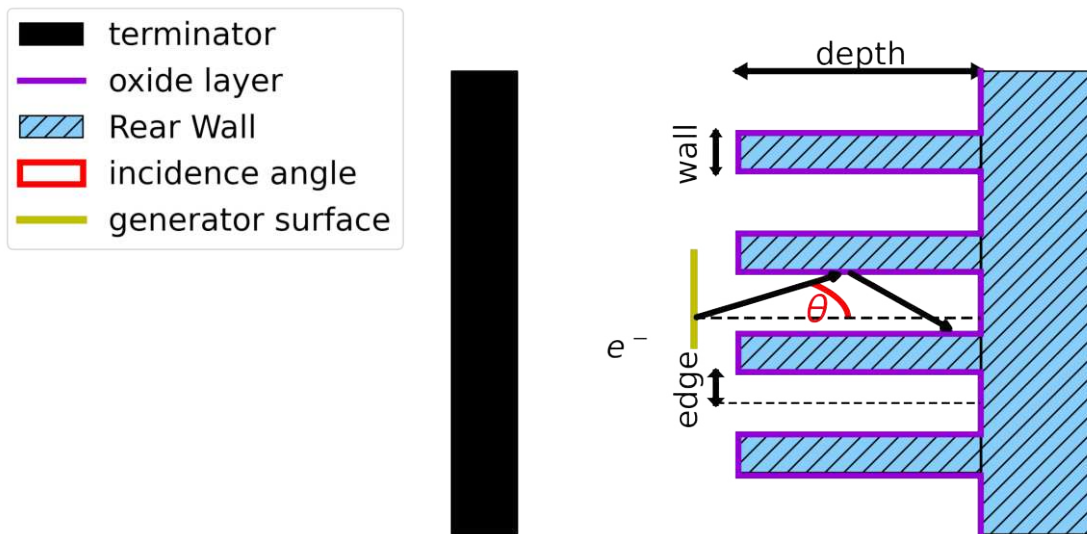
The first comparison between a flat and various micro-structured RWs was done with a metric defined as the weighted backscattering probability. This is calculated using the backscattering probability of each bin P_{E_i, θ_j} , which is then folded with the theoretical tritium β -spectrum taken from the TRModel [25] and the expected angular distribution of the electrons at the RW (see Figure 6.2). This angular distribution originates from an isotropic distribution of the electrons at the source and takes into account the change of the magnetic-field strength during their propagation to the RW. This can be calculated using the following equation [39]:

$$\theta_f = \arcsin \left(\sqrt{\frac{B_f}{B_i} \sin(\theta_i)^2} \right) \quad (6.1)$$

Here, θ_i is the angle of the electron in the original magnetic field B_i and θ_f is the angle of the electron in the final magnetic field B_f . To get the distribution for θ_f , an isotropic source is assumed, which results in the distribution seen in Figure 6.2a. Each bin of the backscattering probability is then multiplied by its corresponding value of the tritium β -spectrum and the angular distribution. Both spectra used for this are shown in Figure 6.2. This is then summed up and normalized to receive a percentage value that will in



- (a) Setup of backscattering simulation with a micro-structured RW with the terminator on the left, the RW segment on the right, and the starting surface distribution of the electrons in the middle. The surface shows an expansion in z -direction for visibility. However, in simulations all electrons start at the same z -position.



- (b) Sketch of the micro-structured RW simulation setup. Magenta is the oxide layer with a given thickness, the RW is lightblue, the detector where electrons are terminated in the simulation is black and will be called terminator to avoid confusion with the KATRIN detector. The definition of the incidence angle is shown in red. The surface, where the electrons are started in the generator is shown in yellow.

Figure 6.1.: Layout of the micro-structured RW in 2D and 3D

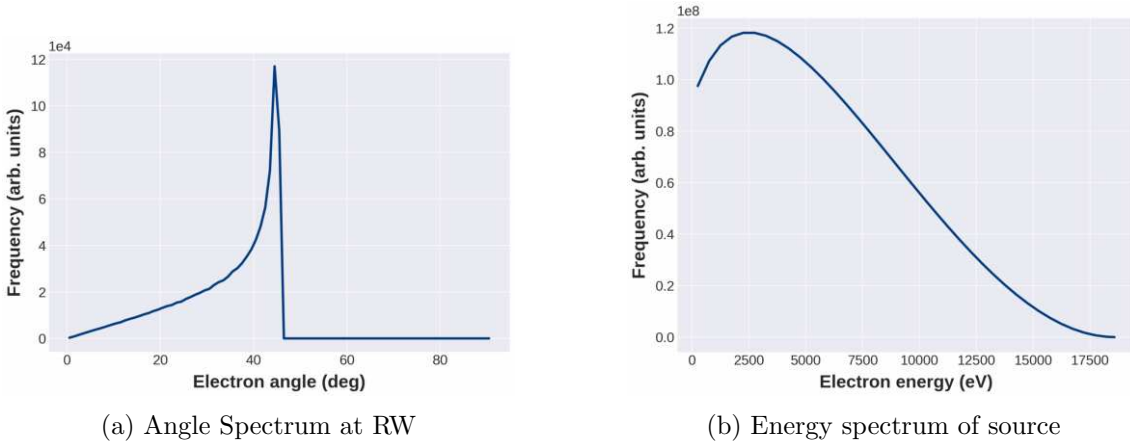


Figure 6.2.: Angle and energy spectrum for calculation of FPD reachable electrons. Angle and energy spectrum used for calculation of FPD reachable electrons. Beta spectrum is taken from TRModel and angle spectrum results from an isotropic source which is changed during the propagation in a changing magnetic field according to equation (6.1).

the following be referred to as the effective backscattering probability which results in the equation:

$$P_{\text{eff}} = \frac{1}{N_{e^-, \text{total}}(E)N_{e^-, \text{total}}(\theta)} \sum_i \sum_j a(E_i, \theta_j) \cdot N_{e^-}(E_i) \cdot N_{e^-}(\theta_j) \quad (6.2)$$

Here, $a(E_i, \theta_j)$ is the backscattering probability for a given starting energy E_i and incident angle θ_j , $N_{e^-}(E_i)$ are the number of electrons the corresponding bin of the tritium decay spectrum and $N_{e^-}(\theta_j)$ is the same for the expected angle spectrum at the RW. $N_{e^-, \text{total}}(E)$ and $N_{e^-, \text{total}}(\theta)$ are the total number of electrons in the angle and beta spectrum and are used for normalization. However, this does not take into account the acceptance angle cut or other effects such as multiple backscatterings and reflections in the KATRIN experiment. Therefore, this is only a rough estimate of the number of electrons that could reach the FPD and should be treated as such. It will only be used to compare the different RWs and to estimate the impact of the RW modifications on the sensitivity, the software TRModel will be used instead (see 6.3). The energy and angle distributions used for this metric are shown in Figures 6.2b and 6.2a. The comparison of different geometries and materials will be shown in the following sections with a focus on the flat and the pTEF structure.

6.1.2. Comparison of Materials and Geometries

The material of the KATRIN RW is one of the most important factors for the backscattering of electrons (see also 4.2.3). Therefore, the backscattering probability of different materials was simulated and compared with that of the current material, which is gold. As explained in section 4.1, the backscattering coefficient is approximately proportional to the atomic number of the material Z (see eq.(4.8)). Thus, beryllium and silicon were chosen as possible materials for the RW because they have a lower atomic number than gold. Beryllium is especially interesting for a RW material due to its low atomic number of 4 which also results in the previously shown low backscattering probability in figure 4.4. However, beryllium is toxic and difficult to handle because the creation of dust must

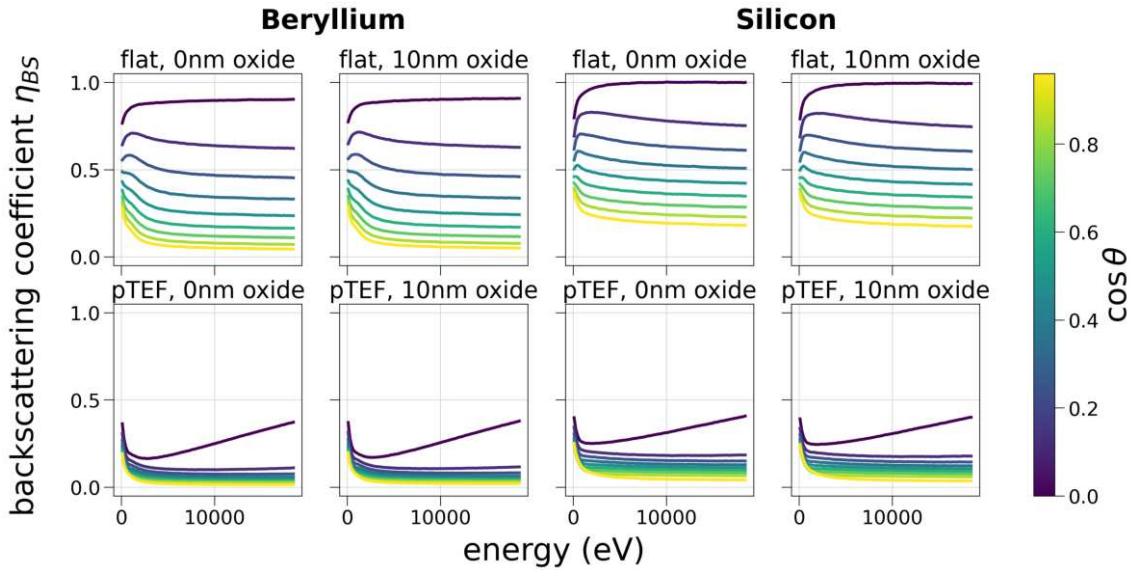


Figure 6.3.: Backscattering probability depending on the incident energy and angle for pTEF and flat geometry for Beryllium and Silicon

be avoided during the manufacturing process. Nevertheless, a Beryllium prototype and several smaller samples have been produced. At the time of writing, these are used at the Tritium Laboratory Karlsruhe (TLK) to investigate Berylliums properties and its applicability for KATRIN with respect to tritium adsorption and electrical conductivity. Silicon, on the other hand, is a safe material with an atomic number of 14 that is still lower than that of gold but worse than beryllium. However, silicon is the most prominent material in the semiconductor industry and is very easy to manufacture because of the existing infrastructure. Due to the use of silicons in semiconductor detectors such as the current FPD and the TRISTAN detector, its backscattering properties are much better understood and have been characterized experimentally within the collaboration [55]. Due to the established infrastructure, micro-structuring of silicon is also a comparatively easy process using the well-known lithography techniques. Beryllium probably would not allow for the same micro-structuring as silicon because the manufacturing process that is designed for silicon. Nevertheless, the comparison presented here includes flat RWs made of gold, beryllium, as well as several varieties of micro-structured ones for Beryllium and Silicon.

The first interesting result of these backscattering simulations is the comparison of the energy and angle spectrum of the different materials. This is shown in figure 6.4. Here, it is visible that the shape of the angle and the energy spectrum is almost the same for all materials, with a difference in the number of backscattered electrons. This is expected as the backscattering probability is related to the atomic number of the material. The next plot to look at is the figure 6.4. Here, the outgoing angle spectrum shape from the two pTEF structured RWs is very similar, however, with a difference in the total number of backscattered electrons. The two flat RWs show a more dissimilar behavior, with the beryllium outperforming the silicon and both having a differing shape. This could be due to the differing form factors explained in Section 4.1 and the different atomic number of the materials.

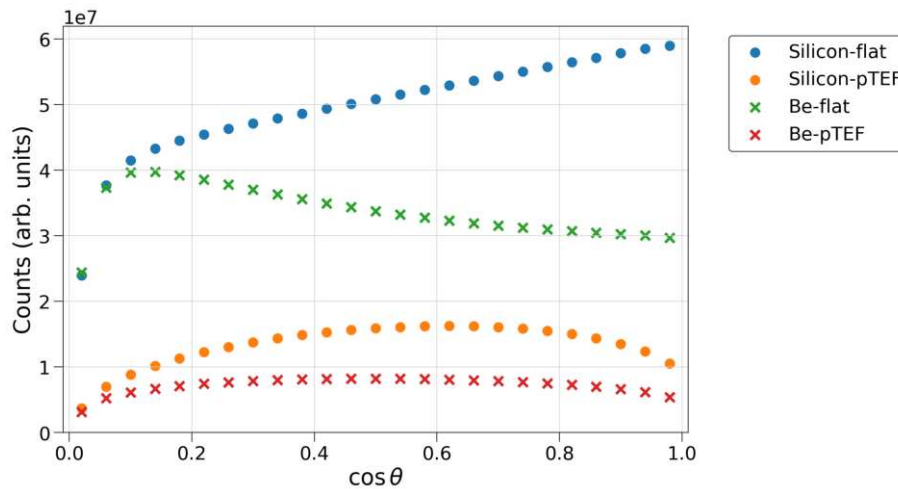


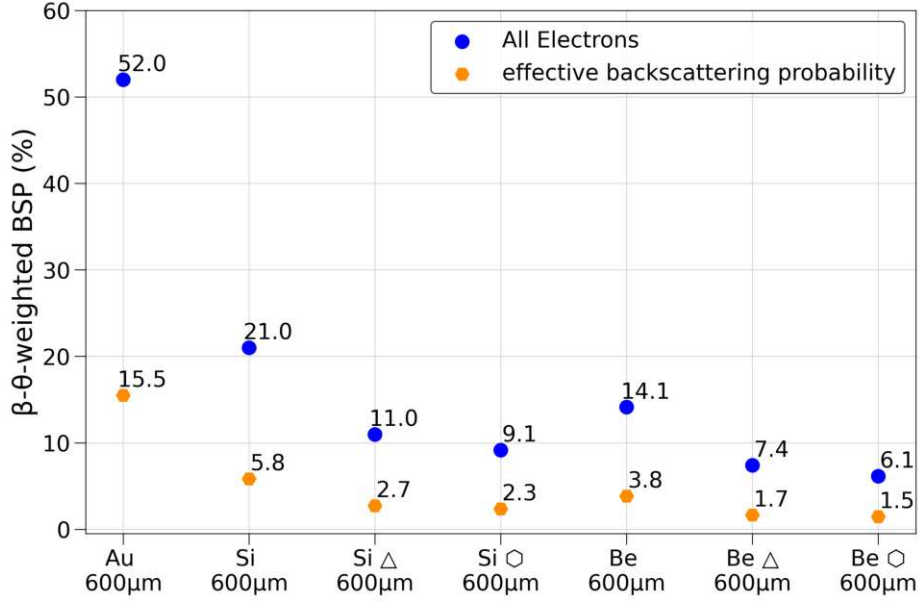
Figure 6.4.: Outgoing angle distribution of all backscattered electrons independent of the energy and input angle (uniform distributions for energy in $[100 \text{ eV}, 18\,600 \text{ eV}]$, and $\cos \theta$ in $[-1, 0]$). $\cos \theta = 1$ ($\theta = 0^\circ$) is parallel to the field lines (z-axis) in the direction toward the KATRIN detector and $\cos \theta = 0$ ($\theta = 90^\circ$) is perpendicular to the field lines.

After discussing the outgoing angle distribution, one can now compare the overall backscattering probability of these combinations. This is shown in figure 6.5a with a comparison being made for flat gold, flat beryllium, and a structured and unstructured silicon RW. The pTEF beryllium RW is left out of this comparison because the manufacturing of such a structure is not possible with the current knowledge of the KATRIN collaboration. The results show that the pTEF silicon RW performs the best out of all combinations, closely followed by the flat beryllium RW. However, as expected, all materials outperform gold by a large margin. Thus, this simulation yields promising prospect for the implementation of a new RW at KATRIN.

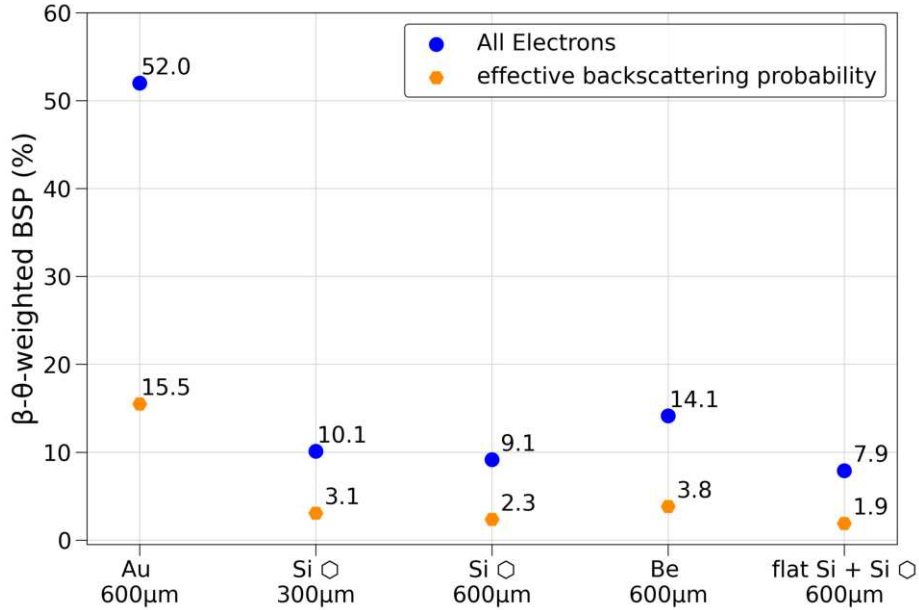
These simulations for a structured RW were also made for multiple depths of the channels. The number of backscattered electrons is antiproportional to the depth of the channels, which means that a higher depth results in reduced backscattering, as shown in 6.5b. The same plot also shows the result for a combination of a silicon RW with a silicon pTEF filter. However, the results are similar, but the increased surface area that comes with such a structure makes this solution more prone to an increased surface activity, which is further researched for the micro-structured RW in Section 6.2. However, the depth scaling is not linear and seems to have an asymptotic behavior. The computation time on the other hand, increases significantly with depth due to the increase in the propagation length of the electrons. Therefore, a depth of $600 \mu\text{m}$ and an edge length of $100 \mu\text{m}$ were chosen for all simulations which is a good compromise between simulation time and reduced backscattering probability. In addition, the depth of the channels is also limited by the manufacturing process of such a structure to about a maximum of $725 \mu\text{m}$ for the Deep Reactive Ion Etch (DRIE) process which is currently being used for the first samples at KATRIN to create such a structure [56].

As mentioned before, the numbers presented in this section only provide a rough first

estimate of the impact of the material and geometry on the sensitivity of the keV-sterile neutrino search to save computational cost. Further comparisons and sensitivity estimates are made using the TRModel in Section 6.3. Compared to the first-order approximation for the FPD reachable RW electrons from eq. (6.2), TRModel properly takes the transport of RW electrons along the beamline into account, including manifold field reflections and RW backscatterings until all electrons are absorbed either at the detector or the RW.



(a) Comparison of different materials and different structures. (\odot) next to the name represents the pTEF structure and (\triangle) next to the material represents an inverted pyramid structure. The pTEF structure performs better, therefore the inverted pyramid structure is not shown in the following plots. As expected micro-structures outperform flat structures and materials with a lower atomic number outperform materials with a higher atomic number. All simulations were done without an oxide layer.



(b) Investigation of channel depth impact for silicon. (\odot) next to the name represents the pTEF structure while number in μm below material describes the depth of the channels. The results also show the combination of a flat silicon RW combined with a pTEF filter in front of the RW also made out of silicon, that performs similar. Results for the pTEF with a flat RW simulation are taken from [57]. As expected, a deeper structure results in a lower backscattering probability. All simulations were done without an oxide layer.

Figure 6.5.: Comparison of different materials and geometries in terms of backscattering probability. A first-order distinction is shown between all backscattered electrons and those that are expected to originate from the WGTS

6.2. Surface Activity Simulations

The tritium activity accumulation on the RW is a major concern for the micro-structured RW due to the increased surface area. This section will mainly focus on the setup of the simulation and direct results. The activity of the RW in terms of its significance as a systematic effect is discussed in sections 3.2.1 and 6.2.1.

The setup of the simulation is in large partes taken from the backscattering simulation, with the only differences being that the electrons are not started at a certain distance with specific angle and energy but are instead started at random positions inside of the RW up to a depth of 10 nm with a homogeneous spatial distribution. The energy distribution is extracted from the theoretical tritium β -spectrum provided by TRModel and the angle distribution is isotropic. This means that no decays are simulated due to its complexity in Geant4 but instead the electrons are started directly. This is a valid assumption as the electrons have a much higher spatial range inside the material than the daughter nuclei and are therefore able to leave the RW and the neutrinos are anyways not detectable in the experiment due to their low cross section.

Another significant change is the choice for the particle generator in Geant4, that is used to initiate the electrons. Previously, the G4ParticleGun class was used, which is very easy to use for simple setups, but lacks some of the more advanced features the G4GeneralParticleSource class provides. The most critical ones for this simulation are the confine method, which allows to confine the generation of particles to specific physical volumes, and the ability to take in an energy distribution from which the energy of the particles is drawn. This is especially useful for the energy distribution of the electrons, which is taken from the theoretical tritium β -spectrum provided by TRModel and to limit the creation of particles to a small depth inside of the RW without writing a complicated custom generator. The number of micro-structure cells to simulate is also limited due to the computational cost of the simulation. Therefore, only one cell with activity is simulated. In particular, the active cell is placed in the middle of six surrounding cells without activity. Apart from the generator, it is essentially the same as the backscattering simulation setup. With this setup the activity of the RW can be simulated with low computational cost and the results can be used to estimate the fraction of electrons that escape the RW, as well as their energy and angle distribution.

6.2.1. Tritium Deposition Mechanisms

The focus will now shift to the mechanisms of tritium deposition at the RW. Currently, it is not fully understood how tritium is deposited, but there are several mechanisms which are considered to be the most likely. There are two known mechanisms that contribute to the deposition of tritium at the RW [25]. The first is due to ions that are guided by the magnetic field to the RW. Their implantation is then determined by the RW field, which repels or attracts them depending on their charge. The second mechanism originates from the non-negligible tritium gas pressure at the RW at nominal column density. This amounts to 4×10^{-6} mbar according to simulations [58]. The type of deposition mechanism

may play a role for the homogeneity of the tritium adsorption at the RW. For example, if ions are the dominant activity source, the tritium may preferably be adsorbed deeper inside the micro-structure channels than in case of neutral gas adsorption. In that case one may hypothesize that the micro-structure can contain the activity better. On the other hand, the micro-structure offers about one order of magnitude more surface area. Therefore, it may adsorb more activity in case of neutral tritium adsorption. Since specifics about the deposition are unknown, a homogeneous spatial distribution is assumed.

These two effects cause an accumulation of tritium over time, leading to significant amount of tritium β -electrons from the RW. Previous studies have shown that the preferred adsorption process for the neutral gas is chemisorption [59][60], but there have been no conclusive results on the location or chemical composition of the tritium at the RW so far [61]. However, the current hypothesis is that tritium is bound to hydrocarbon contaminants which are stuck to the surface of the RW [62]. This idea originates from the development of ozone cleaning explained in Section 3.2.1 which showed the effective removal of 99.9% of the tritium at the RW [62]. During cleaning the activity follows an exponential decay law as a function of ozone exposure time [34].

Before cleaning, the tritium activity amounts to a low percentage value of the total tritium activity in the source with a strong dependence on the last cleaning date [34][33]. In addition to the unknown energy shift from final state excitations, the exact shape of the RW spectrum is still unknown as well [25]. Because of limited statistics and measurement range, such a measurement is currently hard to accomplish, which makes the current modeling attempts even more important, and will be discussed in this section.

6.2.2. Comparison Flat and Micro-structured Rear Wall

In terms of the activity for different geometries, it is currently still unclear how an increased surface in the case of a micro-structure would change the activity of the RW. Therefore, this section will mainly cover a comparison of the energy and angle distribution differences between the flat and pTEF RW. Assumptions on the increase will be made in section 6.3 to estimate the impact of the micro-structure on the sensitivity of the KATRIN experiment.

The first comparison between the two geometries is the starting position of the electrons that reach the terminator inside the RW. In the case of the flat RW, this is rather simple due to the homogeneous distribution inside of the first 10 μm . Due to the low nuclear charge of silicon, most electrons that have a starting angle pointing inside the RW will be absorbed and terminated there as a result of energy loss. Most other electrons can leave the RW almost unhindered. The outgoing activity spectrum could therefore in principle be approximated as one angular hemisphere ($\theta < 90^\circ \rightarrow$ directed away from RW bulk) of almost unscattered electrons, plus one hemisphere ($\theta < 90^\circ \rightarrow$ directed toward RW bulk) of backscattered electrons.

For the pTEF, the starting position distribution is not as simple. In total, most electrons start inside the walls of the hexagonal cell due to its large surface area. However, the starting height shows two peaks at the top and bottom of the cell. These originate from

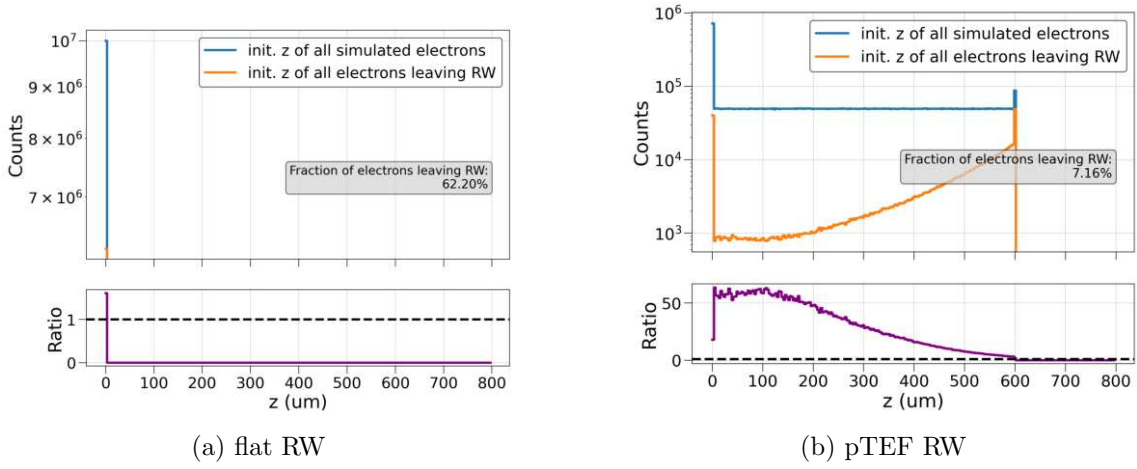


Figure 6.6.: Starting height distribution for flat and pTEF RW for silicon with ratio plot of all started electrons and electrons leaving the RW

the large areas at the bottom of the channel and on the walls which connect the cells. In the case of the bottom, the number of electrons that can leave the channel is rather low compared to the total number of the ones that started with 7.16%. But at the walls connecting the channels, most electrons are able to leave the RW unhindered because they do not scatter inside the channel and behave equivalent to the flat RW. The comparison of flat and pTEF RW is shown in figure 6.6. In the case of the flat RW, more than half of the created electrons are able to leave the RW because of backscattered electrons which started in the opposite direction from the terminator and all electrons are very close to the surface. However, this does not take into account the increase in surface area of the structure, and both simulations used ten million electrons.

Another thing to look at is the energy and angle distribution of the primary electrons which leave the RW. This is shown in Figures 6.7 and 6.11. Here, it is visible that the shape of the energy distribution is very similar between the two geometries. The final energy distribution of the electrons leaving the RW shows an increase in the low energy region when compared to the initial energy distribution of the same electrons. This is due to scattering interactions associated with a loss of energy, which is shown by an increase in the low energy region for the pTEF structure, while the flat structure shows a rather flat curve. This can be explained by more scattering in the pTEF structure.

In the case of the angle distribution, the pTEF RW shows a more significant difference to the flat RW. Especially for higher angles, the pTEF shows a more significant reduction and a different shape of the distribution as seen in Figure 6.11. It is also notable that for very low angles close to $\cos \theta \approx 1$ the pTEF shows a visible reduction, which is unexpected at first. However, this originates from the definition of the angle, which is defined by the angle between the momentum and the normal vector of the terminator. Therefore, electrons created in the wall of the hexagonal cell would have to travel a longer distance to leave the wall to achieve such an angle.

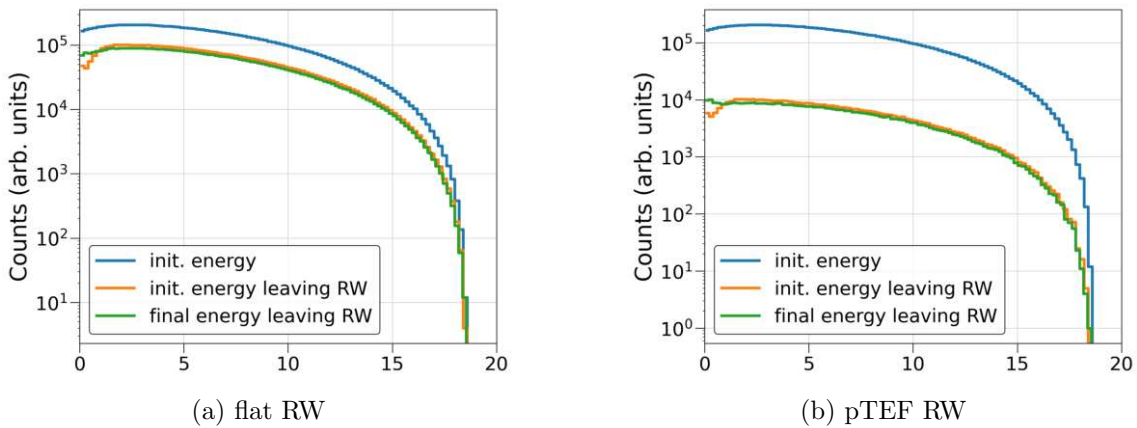


Figure 6.7.: RW activity energy distribution for flat and pTEF RW for silicon of all primary electrons and primary electrons leaving the RW. These distributions include the initial energy distribution of all primary electrons, primary electrons leaving the RW and the final energy of the primary electrons leaving the RW. A larger decrease of electrons across the whole energy range is visible for the pTEF RW.

6.2.3. Comparison of Materials

After comparing the different RW geometries, it is also necessary to compare these geometries while using different materials. The focus will be on the two most probable candidates, beryllium and silicon. In regards to the starting position, final energy and angle distribution of the electrons that leave the RW, the two materials show very similar behaviour with a few key differences. This is shown in Figures 6.8, 6.9, and 6.11.

The first metric to compare is the starting position of the electrons that leave the RW. This is shown in figure 6.8 and there is almost no difference between the two materials with a ratio of about one. The only visible difference is a small drop in the number of electrons for the pTEF structure in the ratio. This means that less electrons for the beryllium RW are able to leave the RW compared to the silicon which is due to the different backscattering probability of these materials. Electrons created at the bottom of the hexagonal cell with an angle parallel to the ground are more likely to be absorbed in the beryllium RW than in the silicon RW.

The next thing to look at is the energy distribution. Here, the energy distribution is almost identical as well, with a difference in the low-energy region for both structures and in the endpoint region for the pTEF. The difference in the low-energy region is due to the differing amount of secondaries produced in the two materials. This could be because of multiple reasons like the higher range of electrons in beryllium. Therefore, low energy electrons are able to leave the bulk before being terminated due to energy loss. The figure 6.10 shows all secondary electrons originating from ionization as well as the auger effect. While the difference in the low energy region can be explained by secondaries, the fluctuations in the higher-energy region in Figure 6.10 are likely due to statistical fluctuations because of insufficient primary electrons of ten million which was limited by computational cost. The difference in the endpoint region in Figure 6.9 is due to insufficient statistics for the pTEF structure with only 7.16% of all simulated electrons leaving the RW.

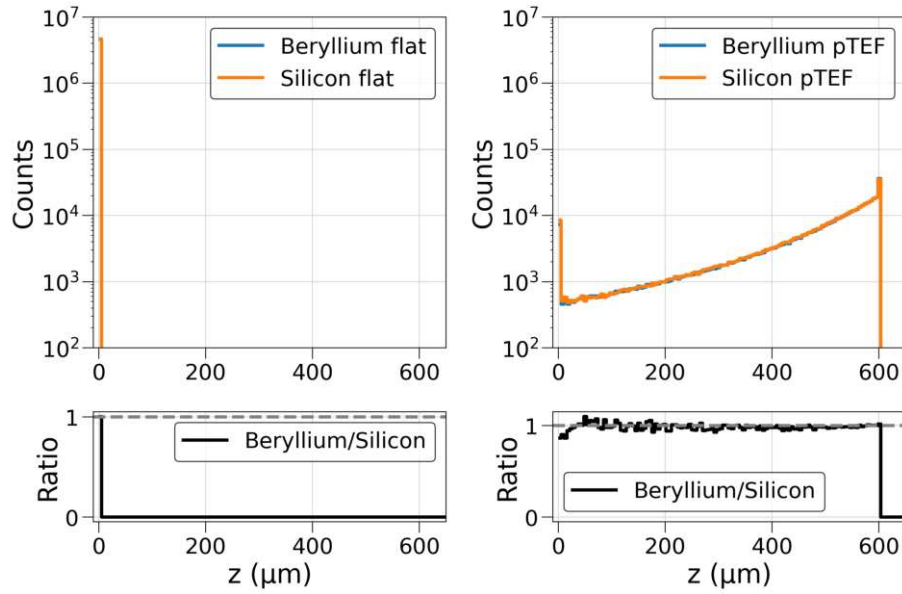


Figure 6.8.: Comparison of the starting height of electrons leaving the RW for beryllium and silicon

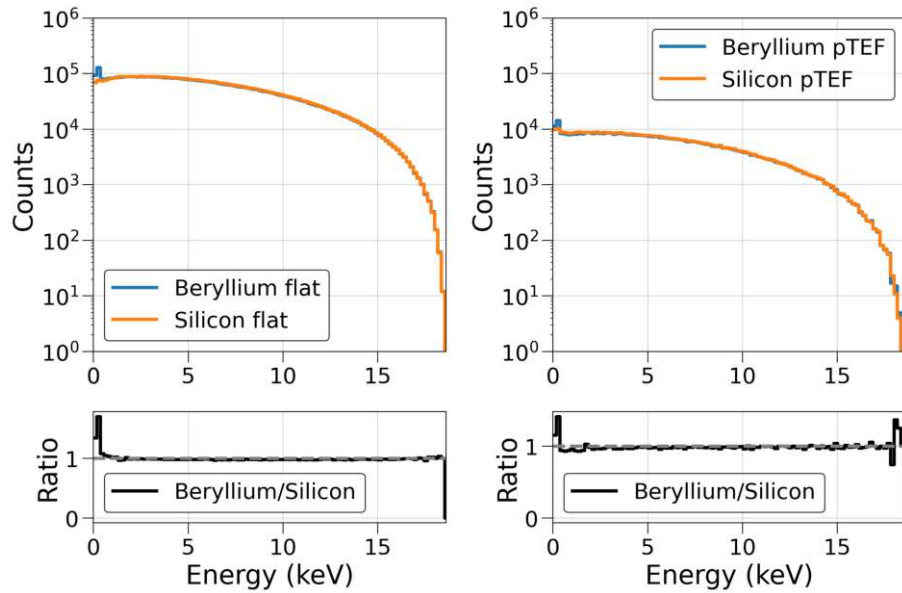


Figure 6.9.: Comparison of the final energy of electrons reaching leaving the RW for beryllium and silicon

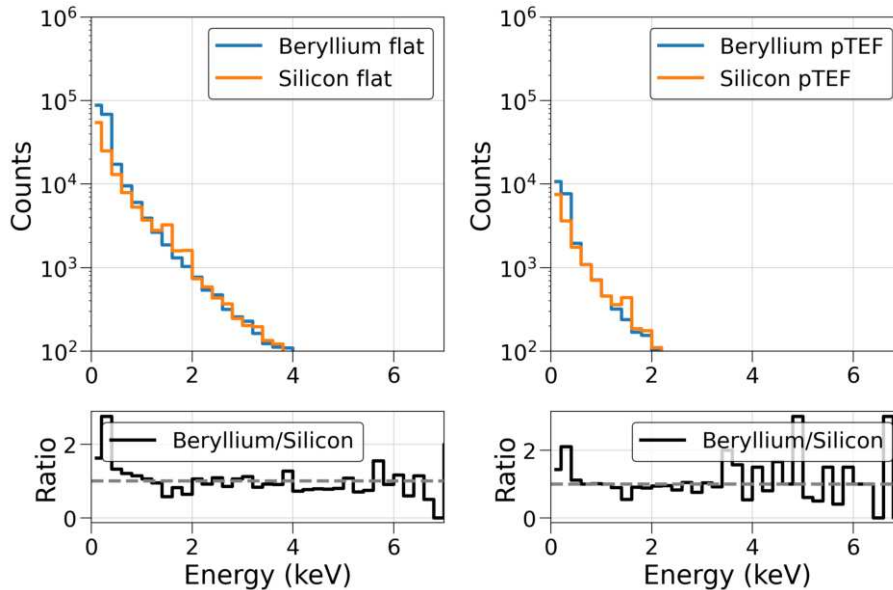


Figure 6.10.: Comparison of the energy distribution of secondary electrons leaving the RW for beryllium and silicon

The last metric to compare is the angle distribution of the electrons that leave the RW. This is shown in figure 6.11. The first difference is seen in the flat geometry where the beryllium RW shows an increase in the number of electrons with an angle close to $\cos \theta \approx 0$, i.e. perpendicular to the normal vector of the terminator. As previously discussed, the range of these electrons is lower in the silicon compared to the beryllium which is due to the different atomic numbers. In the case of the pTEF structure, the same effect is seen for the lower angles which stems from the electrons which are created on top of the walls. Then follows a drop in the ratio because the scattering probability in the silicon pTEF is higher and afterwards a rise in the ratio which also originates from electron created in the walls. These electrons again have a higher range in the wall of the beryllium and are therefore able to leave the RW.

Even though the manufacturing of beryllium with a micro-structure is unlikely, this materials comparison is crucial for disentangling the effects of the different materials from the micro-structure. The results of these simulations are further used to create activity matrices, which are shown in Figure 6.12. Here, the discussed effects culminate in different inputs later used for the TRModel and therefore different impacts on the sensitivity for the keV-sterile neutrino search.

6.2.4. Limitations and Outlook

Even though the micro-structured RW performs better than just a flat beryllium RW, there are still multiple problems and open questions concerning the micro-structure. The most significant one is the impact of the micro-structure on the sensitivity of the KATRIN experiment due to the deposition of tritium at the RW. Because of the unknown process of tritium deposition, it is still unclear if and how the tritium activity would change with increased surface of such a structure. In the case of the pTEF structure, the surface

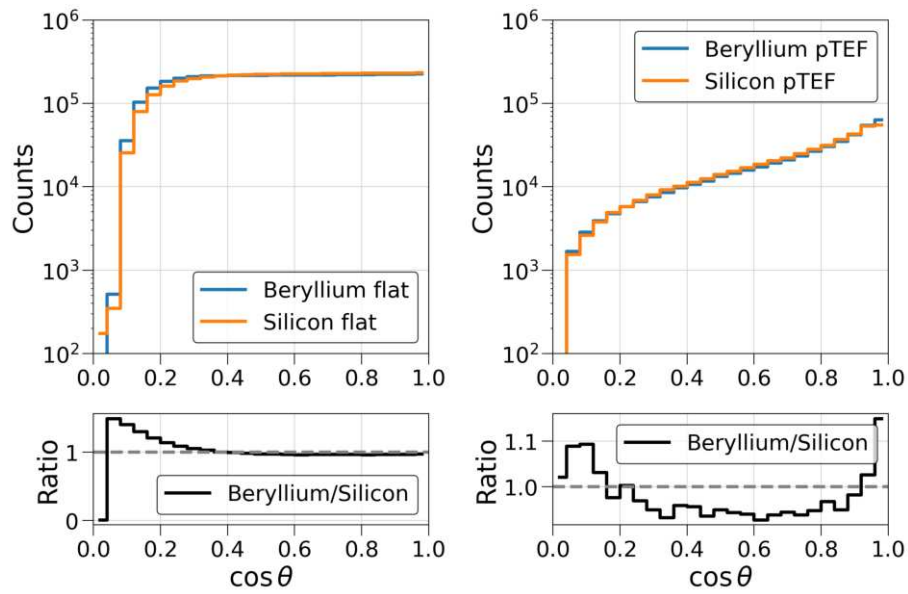


Figure 6.11.: Comparison of the angle distribution of electrons leaving the RW for beryllium and silicon

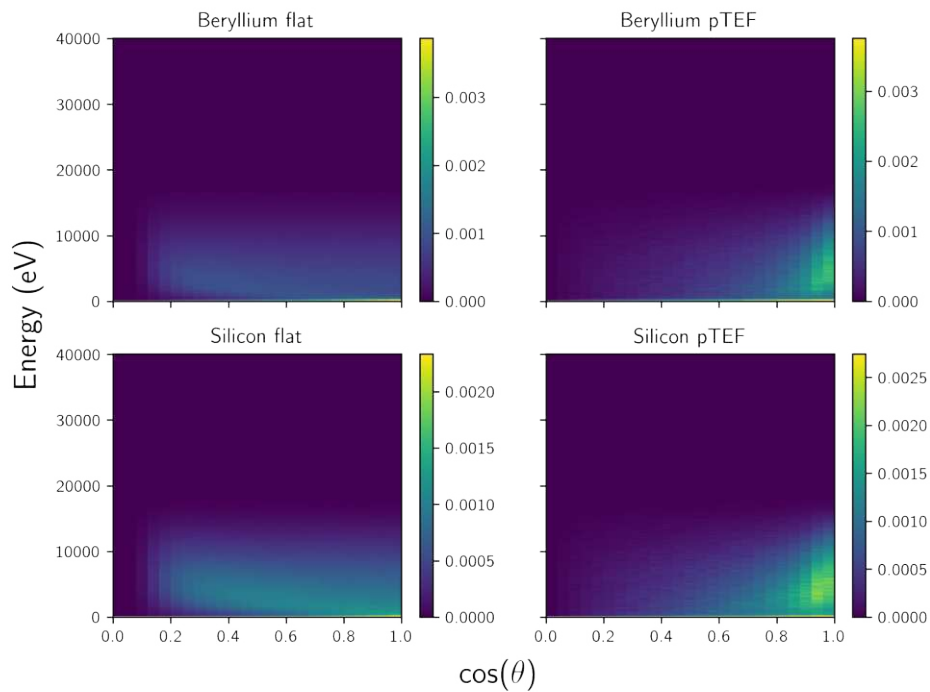


Figure 6.12.: Activity matrices for flat and pTEF RWs for silicon and beryllium. These are used as an input for TRModel.

increase follows the equation:

$$a_{\text{increase}} = 1 + \frac{4ha}{\sqrt{3}(a + d/\sqrt{3})^2} \quad (6.3)$$

Here, a is the edge length of the hexagonal cell, h is the depth of the structure, d is the thickness of the wall and a_{increase} is the factor by which the surface area increases. This results in an area increase of about by a factor of 13.39. If the activity of the RW is proportional to this surface area, the current value of about 1% compared to the total tritium activity in the source would rise to about 13.39% in the worst case, which would significantly affects the sensitivity of the keV-sterile neutrino search. Therefore, it is necessary to investigate how and where exactly the tritium is deposited before the implementation of a micro-structured RW can be decided. However, this is a very complex process and is currently not possible because it is hard to fully mimic the conditions of the rear section and WGTS. At the time of writing, investigations are being performed with neutral tritium gas and without a magnetic field to investigate the behavior of a beryllium and a micro-structured silicon sample [49]. The introduction of a magnetic field and tritium ions may be crucial to fully understand the deposition of tritium on a micro-structured sample due to the different behavior of ion and neutral gas deposition. However, realizing this in a separate test stand would entail a multitude of experimental challenges and may still result in open questions. A test within the beamline itself would provide ideal conditions. However, this may also be challenging since it would require opening the first containment of the tritium loop several times to compare samples.

6.3. Impact on the measured β -decay Spectrum

In this section, the impact of the RW modifications on the sensitivity for the sterile neutrino search will be discussed and compared using sensitivity plots created with TRModel.

6.3.1. Backscattering Contribution

The first thing to be discussed is backscattering. For this, the previous backscattering simulations were used to calculate a response matrices for different materials and structures. This was done by calculating the probability distribution of the outgoing particle for each energy and angle bin with a binning from 100 eV to 40 060 eV with a bin width of 185 eV in energy and from $\cos \theta = 0.0$ to $\cos \theta = 1.00$ with a bin width of $\Delta \cos \theta = 0.04$ in angle. The backscattering matrices were then compared with those currently in use - these were simulated by D. Batzler. The comparison showed only small differences in the low-energy region which could be attributed to different Geant4 versions and its handling of secondaries [63]. A comparison of the result of the previous simulations with the ones created in the context of this thesis is shown in figure 6.13. Here, the response was used as an input for TRModel to compute the differential energy spectrum of the tritium β -electrons that ultimately reach the detector at the end of the KATRIN beamline. The calculation proceeds iteratively in order to take field reflections and manifold RW backscattering into account. The model is also capable of tracking which portion of the spectrum comes from

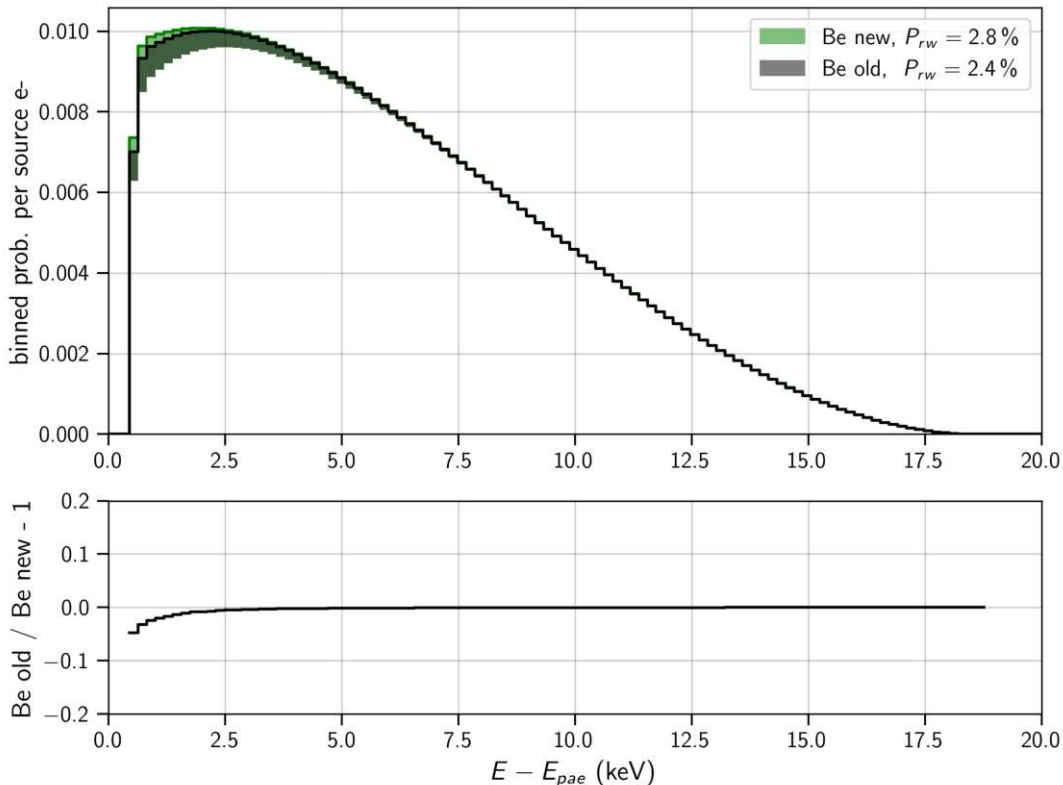


Figure 6.13.: Comparison of the flat RW for simulations that are currently in use in TR-Model and the simulations done in the context of this thesis. Shown is the energy spectrum of the electrons that impinge on the detector at the end of the KATRIN beamline. The shaded region and P_{RW} indicate the portion of the spectrum that comes from electrons that have scattered on the RW at least once. The results are in good agreement with the previous simulations with small differences for the secondaries in the low-energy region due to different Geant4 versions.

electrons that have interacted with the RW at least once (indicated by the shaded region in the spectrum plot). A comparison concerning different RW materials and structures is shown 6.14. Here, it is visible that the beryllium pTEF structure performs the best out of all combinations, followed closely by the silicon pTEF. It is important to keep in mind that the pTEF structure is not possible with beryllium due to the manufacturing process, so the pTEF silicon RW is the best combination if the activity of the RW is neglected. This is also reflected in the sensitivity loss shown in Figure 6.15. Here, the micro-structured beryllium performs best, as previously discussed. However, pTEF beryllium and flat silicon RWs are only included for verification. The two most probable replacements for the RW, the flat beryllium and pTEF silicon RW, show similar overall results. Although flat beryllium performs better than micro-structured silicon in low sterile mass regions, it outperforms beryllium in the higher-mass region. However, as previously discussed, the activity of the RW is already a significant systematic source for a flat RW and would probably be even worse for a micro-structured RW. Therefore, this is further investigated in the next section.

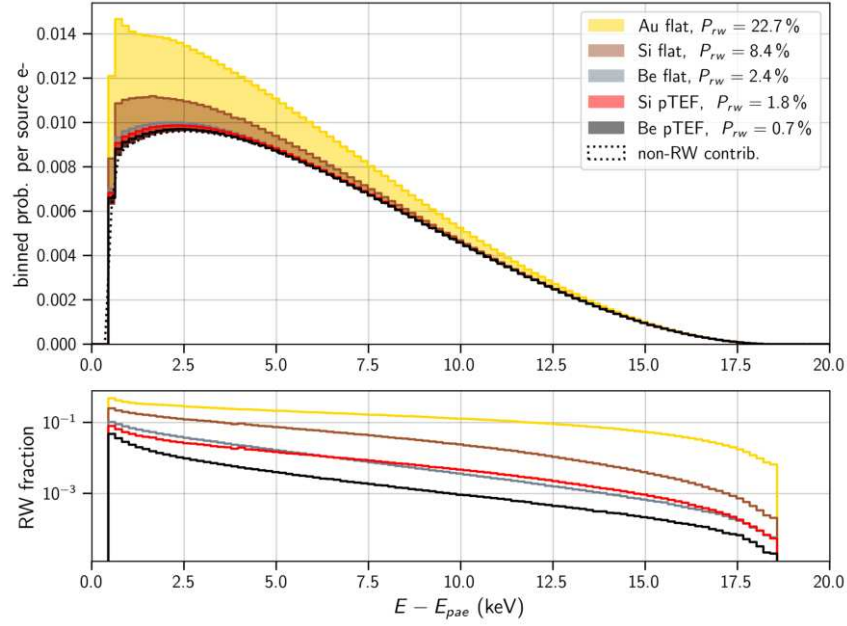


Figure 6.14.: Energy-dependent and total fractions of electrons coming from the RW in the spectrum of incident electrons on the detector for different materials and geometries with backscattering. The pTEF structure performs better than the flat structure and the material with the lowest atomic number performs best in combination with the structure.

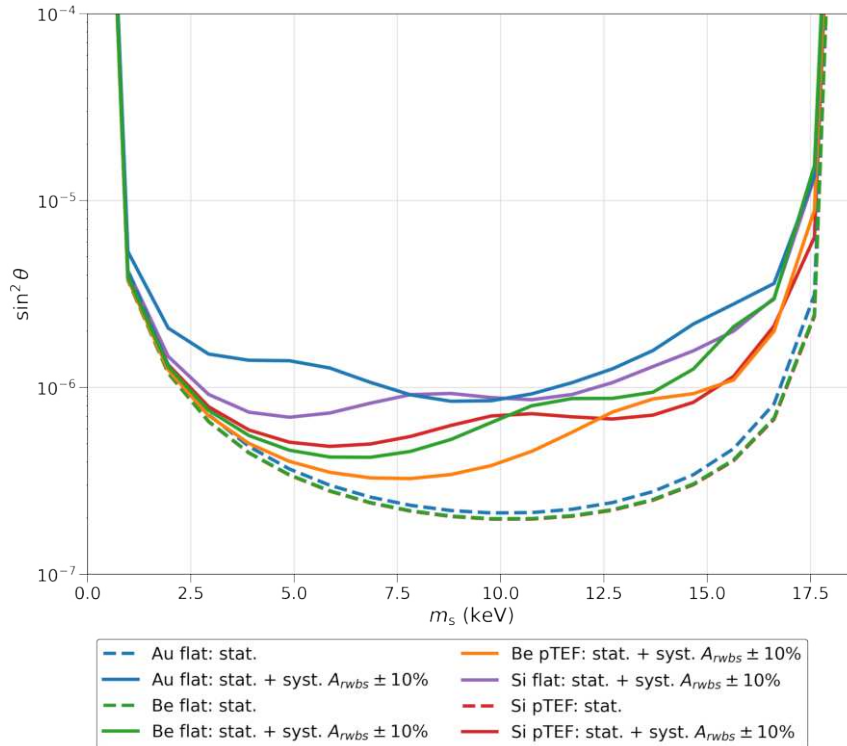


Figure 6.15.: Sensitivity loss for different flat and pTEF geometry with 10% error on the weighing factor A_{rwbs} of the backscattering matrix. Sensitivity with a material with higher atomic number is visible and improvement with the use of micro-structures.

6.3.2. Activity Contribution

To include the activity of the RW in the sensitivity calculation, it is necessary to calculate an energy- and angle-dependent activity spectrum, represented by a 2D matrix for every combination of the geometries and materials. This is done in the activity simulations previously discussed with the same binning as in the backscattering simulations. It was assumed that the tritium atoms are deposited close to the surface with a maximum depth of 10 nm with a homogeneous spatial distribution, which is probably not the case, but is a good first-order approximation because the depth of deposition and its distribution are currently still unknown. In contrast to the backscattering response matrix, the activity matrix is not 4-dimensional but only 2-dimensional, significantly reducing the computation time necessary for the creation.

With these activity matrices, the total fraction of electrons that originate from the RW surface can be calculated in the same way as in case of backscattering and is shown in figure 6.17. Here, it is visible that the pTEF structure performs significantly worse than the flat structures, with the beryllium flat RW performing best, which is contrary to the previous result for only backscattering. This can be largely attributed to the increased surface area, which assumes the worst case of a linear increase of the activity with the area (see eq. (6.3)). It is also interesting to note that the contribution of the RW activity is almost constant across the whole energy range for the pTEF structure. Compared to the flat structure, which decreases for higher energies, this is a significant difference that also shows in the sensitivity loss.

The sensitivity loss caused by these systematics is calculated using the grid scan method from TRModel's sensitivity package. In this method, a χ^2 -test is used to determine the sensitivity for excluding a sterile neutrino signature with a given combination (hypothesis) for sterile mass m_s and mixing amplitude $\sin^2 \theta$. By scanning a grid of hypotheses in the $(m_s, \sin^2 \theta)$ -plane and by comparing the resulting χ^2 -values with the critical value $\chi_{\text{crit}}^2 = 5.99$, a 95% C.L. sensitivity contour is constructed. Further information about the method can be found in [25][47]. For computing the statistical uncertainty, a one year measurement with the fully illuminated TRISTAN detector at an incident electron rate of 10^5 cps per pixel is assumed. The sensitivity impact from systematic parameters is then included with additional covariance matrices in the χ^2 computation. These systematic covariances are estimated by calculating every spectra, where each time the respective systematic parameter is varied. For this, the parameter is drawn from a gaussian distribution with a certain width. Here, the systematic parameters are: the RW backscattering Amplitude A_{RWbs} , which is a multiplicative factor on the overall RW backscattering probability, and A_{RWact} , which is a scaling factor for the injected activity spectrum. The first plot in figure 6.16 shows the sensitivity loss for only the activity of the RW. This shows that the micro-structured RWs perform much worse than the flat RWs, including the gold one for the higher mass range. This would mean that even the current RW could perform better than a micro-structured RW in terms of sensitivity. However, this does not include the full truth because backscattering is not included in this calculation, and gold is mainly a bad choice for the RW due to its high backscattering probability.

The combined sensitivity loss for backscattering and activity is shown in Figure 6.18. Here, gold is performing worse than the micro-structured RWs, which is expected because of the high backscattering probability. However, the flat beryllium RW still outperforms the pTEF RWs including the beryllium pTEF RW. It is also necessary to keep in mind that the assumed error of 10% on the activity would be higher for a higher activity and therefore the sensitivity loss would be higher for the pTEF RWs. But even though these results are assuming the worst case of a linear increase of the activity with the area, the ongoing measurements could possibly not be representative of the true activity of the micro-structured RWs due to the missing magnetic field. There has also been no verification of the simulations done for this thesis and for the energy region with very thin volumes in Geant4 an error of more than 10% should be assumed [53]. So to get a better understanding of the impact of the micro-structured RW on the sensitivity, it is necessary to look into how much the micro-structure can increase the activity without performing worse than a flat beryllium one.

Therefore, the same simulations are made for different scenarios of RW activity. The RW contribution to the total amount of electrons is shown in figure 6.19. Here, it is shown that the pTEF structure performs worse in terms of the RW contribution to the spectrum for all higher activity scenarios over 2% of the WGTS tritium activity. This shows that a slight increase in the activity could be mitigated by the other benefits that come with the micro-structured RW. This, of course, translates to the sensitivity for these scenarios as shown in Figure 6.20. However, as seen in this figure, the flat beryllium still outperforms the silicon pTEF one in the lower mass ranges.

However, such a small increase is not likely due to the large surface increase but depends on the exact mechanism behind the tritium deposition, which is currently unknown. A similar result could maybe be achieved using frequent RW cleaning, but the cleaning in general would have to be tested first, because such a micro-structure could hinder UV light from a point source to reach the whole surface of the RW. Therefore, with current knowledge, the flat beryllium RW is the best choice for the KATRIN experiment in terms of sensitivity, because it is easier to understand in terms of activity. But the micro-structured RWs could be a good choice for future experiments with a better understanding of the tritium deposition mechanisms and the possibility of frequent cleaning.

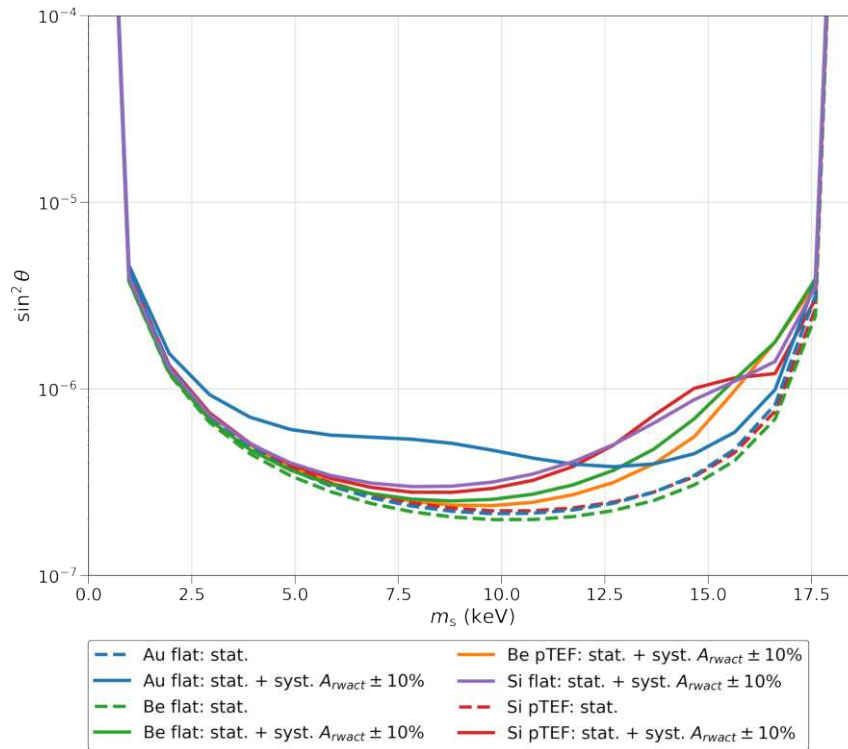


Figure 6.16.: Sensitivity loss for flat and pTEF geometry for different materials with 10 % error on the RW spectrum amplitude A_{rwact} . The RW activity amplitude is 1 % for the flat and 13.39 % for the pTEF RW due to the surface increase which is a result of the micro-structure. The sensitivity loss is much higher for the pTEF structure due to the increased activity.

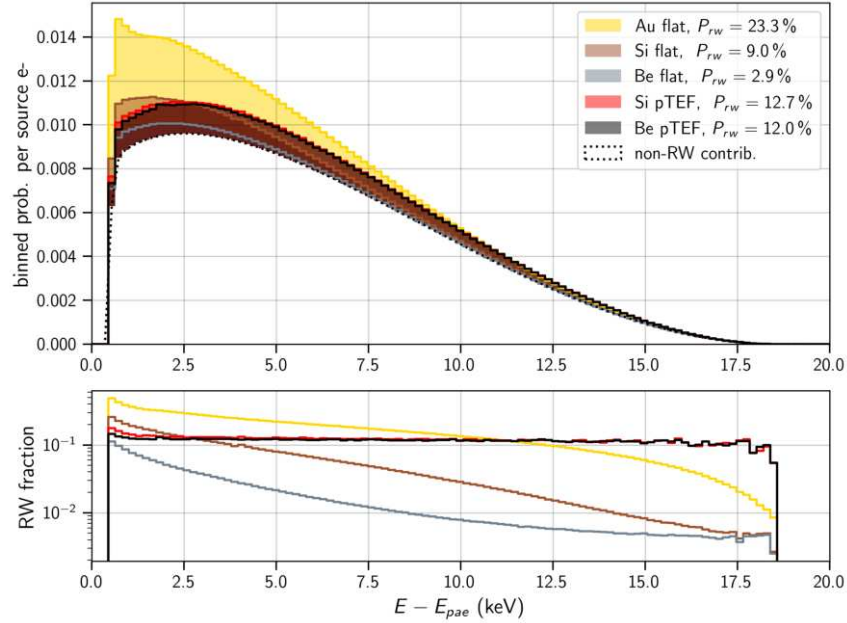


Figure 6.17.: Fraction of electrons coming from the RW for different materials and geometries with backscattering and RW activity. For the flat geometry has an activity of 1% of the tritium activity of the WGTS is assumed. The pTEF structure follows the assumption of a linear increase of the activity with the area and therefore has a much higher fraction of electrons coming from the RW. So according to eq. (6.3), an activity of 13.39% with respect to the WGTS activity is assumed.

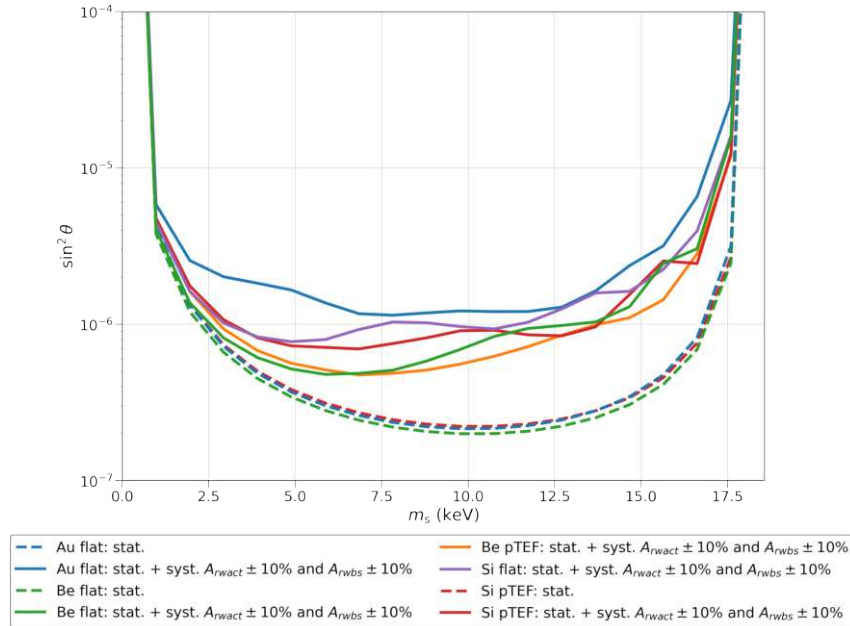


Figure 6.18.: Sensitivity loss for flat and pTEF geometry for different materials with 10% error on the RW spectrum amplitude and the weighting factor for the RW backscattering matrix. As mentioned in figure 6.16, the RW activity amplitude is 1% for the flat and 13.39% for the pTEF RW due to the surface increase which is a result of the micro-structure. The sensitivity loss is much higher for the pTEF structure due to the increased activity. Therefore, the flat beryllium RW performs best on average in terms of sensitivity.

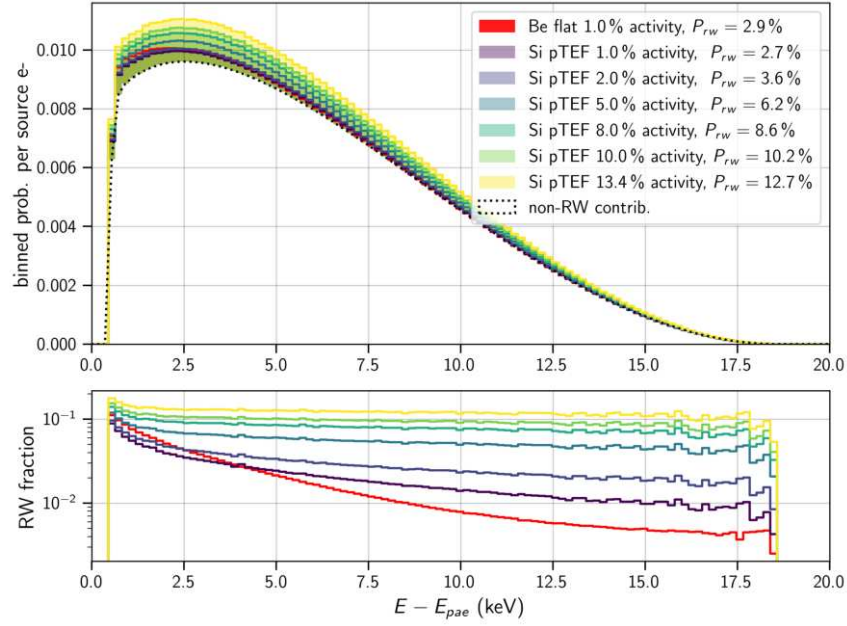


Figure 6.19.: Fraction of electrons coming from the RW for different scenarios of tritium activity originating from the micro-structured RW compared to the flat beryllium case.

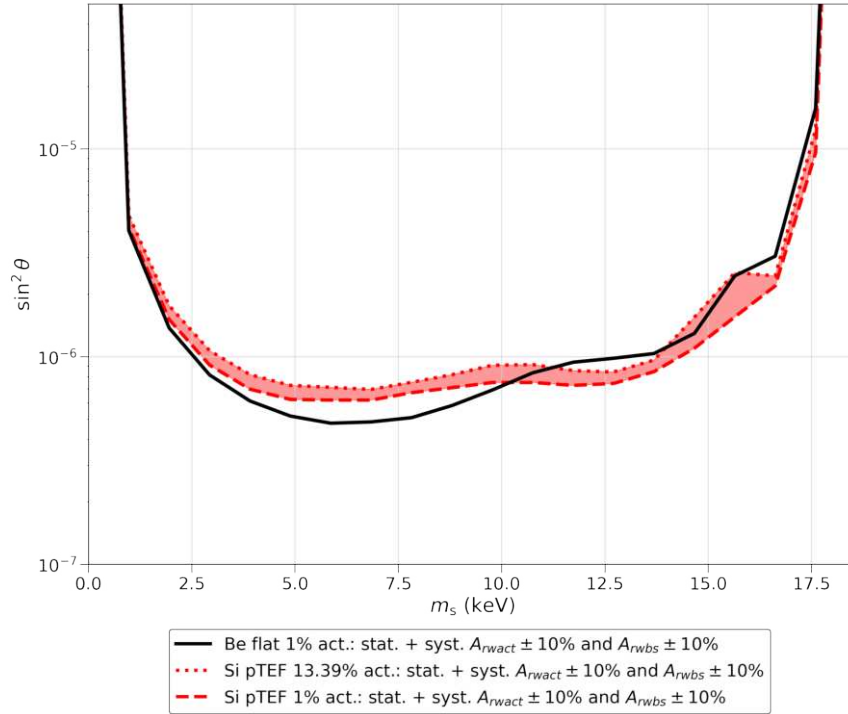


Figure 6.20.: Sensitivity loss comparison between a flat beryllium RW and different activity levels of the micro-structured RW. The red lines are the lower limit of the same activity as the current flat geometry and the upper limit of a linear increase with the area. The colored red area describes the range where different activity levels would be.

7. Conclusion

With the upgrade of the detector and the first phase of TRISTAN, the KATRIN experiment aims to measure the tritium β -decay spectrum with never before seen accuracy to find signs of new physics beyond the Standard Model of particle physics. Currently, the rear wall is one of the biggest contributors to the systematic in the neutrino mass measurement. However, this effect will be even more pronounced in the future keV-sterile neutrino search. This is due to the adjustment of the experiment to measure a broader energy range of the β -spectrum. Normally, the rear wall contribution is reduced by the high retarding potential of the main spectrometer. However, this potential has to be reduced to allow for the deep spectrum measurement which will allow electrons that lost energy during scattering processes at the rear wall to be detected. This includes the electrons originating from the activity of the rear wall itself, and electrons from the WGTS which are emitted towards the RW side or magnetically reflected on the way to the detector because of the isotropic initial angle distribution.

Therefore, this thesis aimed to investigate ways to reduce this rear wall contribution by simulating backscattering and activity characteristics of different rear walls. For one, the rear wall material was changed in dedicated Geant4 simulations and afterwards microstructures were introduced on the rear wall to see how they affect the rear wall contribution. In addition, the effect of the introduction of oxide layers on the different materials was investigated. These oxides could in theory lead to an increase or decrease of the backscattering probability due to the different effective atomic numbers of the oxides compared to the pure materials. However, the results showed no significant difference between the different materials and the different oxide layers for very small oxide layer thicknesses. This is beneficial for beryllium, one of the most promising materials due to its low atomic number, but is unfortunate for the silicon rear wall, which would have a reduced effective atomic number due to the oxide layer. The validity of these results has to be checked by measurements in the future, because very thin volumes can have an ambiguous accuracy in Geant4.

All in all, the simulations showed that the silicon rear wall with a pTEF structure is the most promising candidate in terms of reducing the backscattering contribution of the rear wall. In theory, a micro-structured beryllium rear wall would be even better in this regard,

but the production of such a structure is currently not feasible as discussed in chapter 6.

However, this result changes with the introduction of the rear wall activity. Dedicated simulations showed that the micro-structured plates could possess an activity which, in the worst case, could scale with the surface of such a structure. This would negate the advantages in terms of backscattering and even increase the rear wall contribution for such a structure compared to a simple flat rear wall. In addition, due to the current cleaning method using ozone produced with an UV-lamp, the cleaning could also be a challenge if light is not able to reach inside all of the channels of the micro-structure. Therefore, the introduction of such a micro-structure could come with the risk of increasing the rear wall contribution in the worst case. However, this heavily depends on the tritium deposition mechanism at the rear wall which is currently not understood in terms of where on the micro-structured RW the tritium would adsorb and if a neutral gas or ions are dominant in the deposition process. This would affect the activity because the neutral gas would be able to reach all parts of the structure while the ions would be affected by the magnetic field in the rear section which may affect the spatial distribution of adsorbed tritium.

However, most of these assumptions are currently not backed by measurements, which are currently still ongoing to investigate the beryllium and micro-structured silicon and its interactions with the tritium. However, the measurements lack a magnetic field so ions would not be affected in the same way as in the KATRIN experiment which makes the results hard to interpret for the structured samples.

Something that has also not been taken into account so far is the accuracy of the Geant4 simulations. Typically Geant4 is developed for high energy physics and not for low energy electrons. This can be adapted by choosing the correct models and physics lists, but the accuracy of the results in the low keV energy scale should be expected to have an uncertainty of at least 10%. Without tuning to any measurements, the uncertainty could be even higher.

In conclusion, this thesis proved that the silicon rear wall with a pTEF structure is a very promising candidate for the reduction of the rear wall contribution. However, the currently unknown properties of the tritium deposition at the rear wall and the possible activity increase due to the micro-structure make it hard to predict the effect on the sensitivity loss. Therefore, the flat beryllium rear wall is a safer choice for the keV-sterile neutrino search in the future, as long as no further measurements are available or the deposition mechanism is well understood. Still, the silicon rear wall with a pTEF structure could be a good candidate for the deep spectrum measurement in the future if more knowledge about the deposition mechanism is available.

Bibliography

1. Aker, M. *et al.* Direct neutrino-mass measurement based on 259 days of KATRIN data 2024. arXiv: 2406.13516. <https://arxiv.org/abs/2406.13516>.
2. Hirata, K. S. *et al.* Observation of ^8B solar neutrinos in the Kamiokande-II detector. *Phys. Rev. Lett.* **63**, 16–19. <https://link.aps.org/doi/10.1103/PhysRevLett.63.16> (1 1989).
3. TRISTAN Group. *Conceptual Design Report: KATRIN with TRISTAN detectors* Sept. 2021. [https://www.katrin.kit.edu/downloads/TRISTAN__Technical_Design_Report%20\(10\).pdf](https://www.katrin.kit.edu/downloads/TRISTAN__Technical_Design_Report%20(10).pdf).
4. Pauli, W. *Offener Brief an die Gruppe der Radioaktiven bei der Gauvereins-Tagung zu Tübingen* 1930.
5. Cowan, C. L., Reines, F., Harrison, F. B., Kruse, H. W. & McGuire, A. D. Detection of the Free Neutrino: a Confirmation. *Science* **124**, 103–104. eprint: <https://www.science.org/doi/pdf/10.1126/science.124.3212.103>. <https://www.science.org/doi/abs/10.1126/science.124.3212.103> (1956).
6. Fukuda, Y. *et al.* Evidence for Oscillation of Atmospheric Neutrinos. *Phys. Rev. Lett.* **81**, 1562–1567. <https://link.aps.org/doi/10.1103/PhysRevLett.81.1562> (8 1998).
7. Poon, A. W. P. *Neutrino observations from the Sudbury Neutrino Observatory in AIP Conference Proceedings* **610** (AIP, 2002), 218–230. <http://dx.doi.org/10.1063/1.1469931>.
8. Bellerive, A., Klein, J., McDonald, A., Noble, A. & Poon, A. The Sudbury Neutrino Observatory. *Nuclear Physics B* **908**, 30–51. ISSN: 0550-3213. <https://www.sciencedirect.com/science/article/pii/S0550321316300736> (2016).
9. 2024, N. P. O. A. *The Nobel Prize in Physics 2015* <https://www.nobelprize.org/prizes/physics/2015/summary/> (Accessed: Nov. 13, 2024).
10. Povh, B. & Rith, K. *Teilchen und Kerne* : 9. Aufl. 2014. <http://dx.doi.org/10.1007/978-3-642-37822-5> (Springer Spektrum, Berlin, Heidelberg : 2014).
11. Zuber, K. *Neutrino Physics* <https://directory.doabooks.org/handle/20.500.12854/79366> (Taylor and Francis, 2020).

12. Maki, Z., Nakagawa, M. & Sakata, S. Remarks on the Unified Model of Elementary Particles. *Progress of Theoretical Physics* **28**, 870–880. ISSN: 0033-068X. eprint: <https://academic.oup.com/ptp/article-pdf/28/5/870/5258750/28-5-870.pdf>. <https://doi.org/10.1143/PTP.28.870> (Nov. 1962).
13. Abbasi, R. *et al.* Measurement of atmospheric neutrino mixing with improved IceCube DeepCore calibration and data processing. *Phys. Rev. D* **108**, 012014. <https://link.aps.org/doi/10.1103/PhysRevD.108.012014> (1 2023).
14. An, F. P. *et al.* Precision Measurement of Reactor Antineutrino Oscillation at Kilometer-Scale Baselines by Daya Bay. *Phys. Rev. Lett.* **130**, 161802. <https://link.aps.org/doi/10.1103/PhysRevLett.130.161802> (16 2023).
15. Abe, K. *et al.* Updated T2K measurements of muon neutrino and antineutrino disappearance using 3.6×10^{21} protons on target 2023. arXiv: 2305.09916 [hep-ex]. <https://arxiv.org/abs/2305.09916>.
16. Adhikari, R. *et al.* A White Paper on keV sterile neutrino Dark Matter. *Journal of Cosmology and Astroparticle Physics* **2017**, 025–025. ISSN: 1475-7516. <http://dx.doi.org/10.1088/1475-7516/2017/01/025> (2017).
17. Volkas, R. Introduction to sterile neutrinos. *Progress in Particle and Nuclear Physics* **48**, 161–174. ISSN: 0146-6410. <https://www.sciencedirect.com/science/article/pii/S0146641002001229> (2002).
18. Wickremasinghe, A. *Booster Neutrino Beam* https://indico.fnal.gov/event/8863/contributions/110288/attachments/71809/86170/BNB_NBI_athula_2014.pdf (Accessed: Nov. 13, 2024).
19. Aguilar-Arevalo, A. A. *et al.* Updated MiniBooNE neutrino oscillation results with increased data and new background studies. *Physical Review D* **103**. ISSN: 2470-0029. <http://dx.doi.org/10.1103/PhysRevD.103.052002> (Mar. 2021).
20. Acero, M. A. *et al.* White paper on light sterile neutrino searches and related phenomenology. *Journal of Physics G: Nuclear and Particle Physics* **51**, 120501. ISSN: 1361-6471. <http://dx.doi.org/10.1088/1361-6471/ad307f> (Oct. 2024).
21. Aker, M. *et al.* Improved eV-scale sterile-neutrino constraints from the second KATRIN measurement campaign. *Physical Review D* **105**. ISSN: 2470-0029. <http://dx.doi.org/10.1103/PhysRevD.105.072004> (Apr. 2022).
22. Abazajian, K. N. Sterile neutrinos in cosmology. *Physics Reports* **711–712**, 1–28. ISSN: 0370-1573. <http://dx.doi.org/10.1016/j.physrep.2017.10.003> (Nov. 2017).
23. Dessert, C., Rodd, N. L. & Safdi, B. R. The dark matter interpretation of the 3.5-keV line is inconsistent with blank-sky observations. *Science* **367**, 1465–1467. eprint: <https://www.science.org/doi/pdf/10.1126/science.aaw3772>. <https://www.science.org/doi/abs/10.1126/science.aaw3772> (2020).
24. Benso, C., Schwetz, T. & Vatsyayan, D. *Large neutrino mass in cosmology and keV sterile neutrino dark matter from a dark sector* 2024. arXiv: 2410.23926 [hep-ph]. <https://arxiv.org/abs/2410.23926>.

25. Descher, M. *Differential spectrum modeling and sensitivity for keV sterile neutrino search at KATRIN* Phd Thesis (Karlsruher Institut für Technologie (KIT), 2024). 213 pp.
26. Leach, K. G. & Friedrich, S. The BeEST Experiment: Searching for Beyond Standard Model Neutrinos Using ^7Be Decay in STJs. *Journal of Low Temperature Physics* **209**, 796–803. ISSN: 1573-7357. <http://dx.doi.org/10.1007/s10909-022-02759-z> (July 2022).
27. BeEST Collaboration. <https://beest.mines.edu/scientists/> (Accessed: Dec. 13, 2024).
28. Otten, E. W. & Weinheimer, C. Neutrino mass limit from tritium beta decay. *Reports on Progress in Physics* **71**, 086201. ISSN: 1361-6633. <http://dx.doi.org/10.1088/0034-4885/71/8/086201> (July 2008).
29. Mertens, S. *et al.* A novel detector system for KATRIN to search for keV-scale sterile neutrinos. *Journal of Physics G: Nuclear and Particle Physics* **46**, 065203. <https://dx.doi.org/10.1088/1361-6471/ab12fe> (May 2019).
30. KATRIN Collaboration. *KATRIN design report 2004* tech. rep. 51.54.01; LK 01 (Forschungszentrum Jülich, 2005). 245 pp.
31. Kuckert, L. *et al.* Modelling of gas dynamical properties of the Katrin tritium source and implications for the neutrino mass measurement. *Vacuum* **158**, 195–205. ISSN: 0042-207X. <https://www.sciencedirect.com/science/article/pii/S0042207X18310972> (2018).
32. Weidenthaler, M. *Description of the RW systematic* Information in KATRIN Wiki (unpublished). Mar. 19, 2024.
33. Sack, R. *et al.* *Rear Wall status* Presentation at the 44th KATRIN Collaboration Meeting (unpublished). Mar. 8, 2023.
34. App, T. *Experimentelle Analyse eines Reinigungsverfahrens der KATRIN Rear Wall mittels Ozon in eines Teststand* BA thesis (unpublished). Apr. 11, 2022.
35. Aker, M. *et al.* The design, construction, and commissioning of the KATRIN experiment. *Journal of Instrumentation* **16**, T08015. <https://dx.doi.org/10.1088/1748-0221/16/08/T08015> (2021).
36. Klein, M. *Tritium ions in KATRIN: blocking, removal and detection* 51.03.01; LK 01. PhD thesis (Karlsruher Institut für Technologie (KIT), 2019). 340 pp.
37. Gil, W. *et al.* The Cryogenic Pumping Section of the KATRIN Experiment. *IEEE Transactions on Applied Superconductivity* **20**, 316–319 (2010).
38. Friedel, F. *et al.* Time-dependent simulation of the flow reduction of D2 and T2 in the KATRIN experiment. *Vacuum* **159**, 161–172. ISSN: 0042-207X. <https://www.sciencedirect.com/science/article/pii/S0042207X18313873> (2019).
39. Hinz, D. F. *Background systematics and extensions to the KATRIN background model* 51.13.02; LK 01. PhD thesis (Karlsruher Institut für Technologie (KIT), 2022). 157 pp.

40. Aker, M. *et al.* KATRIN: status and prospects for the neutrino mass and beyond. *Journal of Physics G: Nuclear and Particle Physics* **49**, 100501. <https://dx.doi.org/10.1088/1361-6471/ac834e> (Sept. 2022).
41. Amsbaugh, J. *et al.* Focal-plane detector system for the KATRIN experiment. *Nuclear Instruments and Methods in Physics Research Section A: Accelerators, Spectrometers, Detectors and Associated Equipment* **778**, 40–60. ISSN: 0168-9002. <https://www.sciencedirect.com/science/article/pii/S0168900215000236> (2015).
42. Harms, F. T. *Characterization and Minimization of Background Processes in the KATRIN Main Spectrometer* 51.03.01; LK 01. PhD thesis (Karlsruher Institut für Technologie (KIT), 2015).
43. Descher, M. *TRISTAN systematic simulation* THAI-KATRIN School on Neutrino Physics (unpublished). May 8, 2024.
44. Dapor, M. *Transport of Energetic Electrons in Solids* : 4th ed. 2023. <https://doi.org/10.1007/978-3-031-37242-1> (Springer International Publishing, Cham : 2023).
45. National Institute of Standards and Technology. *Composition of Beryllium* <https://www.physics.nist.gov/cgi-bin/Star/compos.pl?mode=text&matno=004> (Accessed: Dec. 9, 2024).
46. Everhart, T. E. Simple Theory Concerning the Reflection of Electrons from Solids. *Journal of Applied Physics* **31**, 1483–1490. ISSN: 0021-8979. eprint: https://pubs.aip.org/aip/jap/article-pdf/31/8/1483/18321956/1483_1_online.pdf. <https://doi.org/10.1063/1.1735868> (Aug. 1960).
47. Trost, K. *Mitigation of Rear Wall Backscattering in keV Sterile Neutrino Searches at the KATRIN Experiment* Master’s Thesis (Karlsruher Institut für Technologie (KIT), July 30, 2024).
48. Arenz, M. *et al.* The KATRIN superconducting magnets: overview and first performance results. *Journal of Instrumentation* **13**, T08005. <https://dx.doi.org/10.1088/1748-0221/13/08/T08005> (Aug. 2018).
49. Batzler, D., Röllig, M. & Sack, R. *Status Update on Rear Wall Qualification Measurements for the KATRIN Experiment* in *47th KATRIN Collaboration Meeting* (Sept. 30, 2024).
50. Geant4 Collaboration. *Book for Application Developers* <https://geant4-userdoc.web.cern.ch/UsersGuides/ForApplicationDeveloper/fo/BookForApplicationDevelopers.pdf> (Dec. 8, 2023).
51. Geant4 Collaboration. *Guide for Physics Lists* <https://geant4-userdoc.web.cern.ch/UsersGuides/PhysicsListGuide/fo/PhysicsListGuide.pdf> (Dec. 8, 2023).
52. Geant4 Collaboration. *Physics Reference Manual* <https://geant4-userdoc.web.cern.ch/UsersGuides/PhysicsReferenceManual/fo/PhysicsReferenceManual.pdf> (Dec. 8, 2023).

-
53. Batic, M., Hoff, G., Pia, M. G., Saracco, P. & Weidenspointner, G. Validation of Geant4 Simulation of Electron Energy Deposition. *IEEE Transactions on Nuclear Science* **60**, 2934–2957. ISSN: 1558-1578. <http://dx.doi.org/10.1109/TNS.2013.2272404> (Aug. 2013).
 54. Ivanchenko, V. *Geant4 Electromagnetic Physics* in (CIEMAT, Madrid, Spain, 2019). <https://indico.cern.ch/event/746466/contributions/3308237/attachments/1833040/3002454/Geant4EMPhysics.pdf>.
 55. Spreng, D. *Electron Backscattering on Silicon Drift Detectors and Its Impact on a Sterile Neutrino Search with KATRIN* Master’s thesis (Department of Physics, Technical University of Munich, Mar. 1, 2023).
 56. Fraunhofer Institute for Silicon Technology. *Deep Reactive Ion Etching (DRIE)* <https://www.isit.fraunhofer.de/en/technology/micro-manufacturing-processes/processes-on-wafer-level/drie.html> (Accessed: Nov. 27, 2024).
 57. Hinz, D. *Microstructured filter for Rear Wall backscattering reduction* Deep Model workshop 2023 (unpublished). Nov. 13, 2023.
 58. Raspopin, E. *Systematic effects of the plasma and surfaces in the KATRIN tritium source* Master’s thesis (Institute for Astroparticle Physics (IAP), KIT, July 14, 2021).
 59. Klein, M. *Adsorption of gaseous tritium on gold coated beryllium investigated with TRIADE* Master’s thesis (Department of Physics, Technical University of Munich, Mar. 31, 2015). https://www.katrin.kit.edu/publikationen/ManuelKlein_math.pdf.
 60. Röllig, M. *Tritium analytics by beta induced X-ray spectrometry* 51.03.01; LK 01. PhD thesis (Karlsruher Institut für Technologie (KIT), 2015). 202 pp.
 61. Aker, M. *et al. Rear wall residual tritium spectrum* https://iap-katrin-wiki.iap.kit.edu/katrin/images/1/14/201011_RW-update.pdf (Accessed: Nov. 10, 2020).
 62. Rear Wall working group. *Rear wall residual tritium spectrum wiki page* https://iap-katrin-wiki.iap.kit.edu/katrin/index.php/RW_residual_tritium_spectrum (Accessed: Dec. 13, 2024).
 63. Batzler, D. *Comparison of Geant4 v10.7.2 and v11.2.0* Deep Model Meeting (unpublished). Jan. 11, 2024.

A. TRModel Simulation Settings

Table A.1.: TRModel components and settings for micro-structured RW simulations.

Parameter/Effect	Parameter name	Added in simulation
Sterile neutrino incl. in theory	theo_add_sterile	True
Small terms incl. in theory	theo_small_terms	True
RW Backscattering	rw_backscattering	Depending on simulation
RW Activity	rw_activity	Depending on simulation
Source Scattering init	src_scattering_init	False
Source Scattering side	src_scattering_side	False
Magnetic traps	prop_magnetic_traps	False
Electrode decay	prop_electrode_decay	True
Detector backscattering	det_qe_backscattering	True
Detector charge sharing	det_charge_sharing	True
Fano noise	det_fano_noise	True
DAQ Threshold	daq_threshold	True
DAQ Deadtime	daq_deadtime	True
Pileup	daq_pileup	True
Electronic noise	daq_electronic_noise	True
Calibration	daq_calibration	True
Back reflection	ref_backreflection	False

Table A.2.: TRModel parameters used for simulations. Only backscattering and activity parameters are changed depending on the simulation. This includes the parameters amp_Bs, amp_Rw and prop_ampRw.

Description	Parameter	Value
Background	glob_bkg	6c-7 cps/eV
Column density	glob_rhod	adjusted for each scenario
Tritium purity	glob_purity	0.95
Pixel efficiency	glob_pxEff	1.00
Number of golden pixels	glob_pxNumber	936
Final amplitude scaling	glob_amp	1.0
Dead layer parameter	det_lambda	58 μm
Charge cloud width	det_ccWidth	20 μm
Pixel radius	det_pxRadius	1500.0 μm
Fano scaling	det_fanoScale	1.0
Detector back reflection scaling	ref_ampBr	1.0
Scattering init	src_rhodInit	5e15 molecules/cm ²
Scattering side	src_rhodSide	5e15 molecules/cm ²
Trap scattering	src_rhodTrap	5e14 molecules/cm ²
RW backscattering Material + Geometry	rw_ampBs1	1.
RW activity spectrum Material + Geometry	rw_ampAct1	1.
RW B field	prop_Brw	1.26 T
Maximum upstream B field	prop_Bmu	3.60 T
Source B field	prop_Bsrc	3.60 T
Maximum downstream B field	prop_Bmd	3.60 T
Detector B field	prop_Bdet	1.40 T
Btrap/Bsrc fraction	prop_Ftrap	0.9920635
Main spectrometer qU	prop_qUms	500 eV
Rear electrode qU	prop_qUre	0 eV
Post acceleration energy	prop_Epae	20000 eV
RW acceleration energy	prop_Erwa	0 eV
RW spectrum amplitude in rel. to WGTS	prop_ampRw	Depending on structure (1% for flat, 13.39% for pTEF)
Reelectrode spectrum amplitude	prop_ampRe	1c-3
WGTS spectrum amplitude	prop_ampSrc	1.0
DAQ gain	daq_gain	1.0
DAQ offset	daq_offset	0.0
Noise width	daq_sigEn	43.74 eV
Minimum resolution time, pileup scaling	daq_tauMin	112 ns
Dead time, spectrum scaling	daq_tauDead	1.15 μs
Reset pulse frequency	daq_rcsRate	1.0e3 Hz
Inhibit time	daq_inhibit	51 μs
Trigger threshold	daq_trThresh	2000 eV
Trigger cutoff	daq_trWidth	150 eV
Pileup amplitude	daq_ampPu	1.0